

Full Length Article

Energy and exergy analyses of novel supercritical CO₂ Brayton cycles driven by direct oxy-fuel combustor

Ahmad K. Sleiti^{*}, Wahib A. Al-Ammari

Department of Mechanical & Industrial Engineering, College of Engineering, Qatar University, Qatar



ARTICLE INFO

Keywords:

Supercritical carbon dioxide
sCO₂
Brayton cycle
Direct oxy-combustion
Exergy

ABSTRACT

This study addresses major research gaps related to supercritical carbon dioxide (sCO₂) power cycles including the shortcomings due to adding extra components, the high operating temperatures and the lack of studies on using direct oxy-combustion for sCO₂ power cycles. Energy and exergy analyses for five novel sCO₂ Brayton cycles with direct oxy-fuel combustion are introduced. The studied cycle configurations are the simple recuperator cycle (SRC), dual recuperator cycle (DRC), intercooling cycle (ICC), reheating cycle (RHC) and partial intercooling cycle (PIC). A numerical model was developed for the detailed calculations of the recuperators that considers variations in the properties of sCO₂ as a function of temperature. Comprehensive studies and optimization are performed for the major parameters including the pressure ratio (r_c), intermediate pressure ratio (RPR), turbine inlet temperature (TIT) and compressor inlet temperature (CIT). Optimum r_c and RPR values have been obtained at which the maximum efficiencies of the cycles occur. Results show that the partial intercooling cycle (PIC) has superior performance compared to the other configurations at higher TIT and lower PRR. The maximum thermal efficiency of 52% is achieved by the PIC at r_c of 5, RPR of 0.45, TIT of 750 °C, high pressure of 20 MPa, and CIT of 50 °C. Furthermore, the reheating cycle has the highest second law efficiency with marginal improvement in the thermal efficiency compared to the dual recuperator cycle (DRC).

1. Introduction

The high thermal efficiency levels, compactness and near zero sCO₂ emissions are the most attractive features of the supercritical carbon dioxide (sCO₂) power cycle [1]. The dense behavior of the sCO₂ near the critical point enables its compression with a significant reduction in the compression power [2]. This particular merit improves the thermal efficiency even at moderate turbine inlet temperatures (TIT). Also, the sCO₂ power cycle has the advantages of high power density and clean and non-toxic working fluid in addition to near zero CO₂ emissions [3]. Moreover, the sCO₂ power cycle can be integrated and combined with variable technologies including concentrated solar power [4–7], waste heat recovery [8–10], Gen IV nuclear reactor [2,11,12], geothermal [13,14], and fuel cell systems [15–17].

In open literature, there are many studies of numerous configurations and layouts of sCO₂ power cycles [1,18]. These studies attempted to improve the performance of the cycle by improving the cycle

processes (such as heat addition, working fluid expansion, heat recovery by high and low temperature recuperators, cooling, and compression processes) or by integrating the sCO₂ cycle with other systems to improve the overall efficiency of the combined system [19,20]. However, significant research gaps are still exist to improve the operation and performance of the sCO₂ power cycle, which will be highlighted in this section. The basic layout of the supercritical CO₂ cycle consists of a compressor, heater, turbine, regenerator, and cooler. In the transcritical version, the gas compressor is replaced with a liquid pump and the cooler is replaced with a condenser [21]. In the transcritical case, the lower pressure of the cycle is imposed by a condenser [22] which is a limitation that can be resolved by involving the precompression process. The regeneration process greatly affects the thermal efficiency of the CO₂ cycles [23]. So, the regeneration process is usually implemented by using two recuperators that operate at a different range of temperatures to reduce the effects of irreversibility. However, some of the investigated layouts in literature include only one recuperator [24,25], or without recuperator [1]. Similar to the improvements of the conventional open

Abbreviations: ASU, Air separation unit; CIT, Compressor inlet temperature; DOC, Direct oxy-fuel combustor; DRC, Dual recuperator cycle; ICC, Intercooling cycle; LHV, Lower heating value of the fuel; LMTD, Logarithmic mean temperature difference; PCHE, Printed circuit heat exchanger; PIC, Partial intercooling cycle; RHC, Reheating cycle; SRC, Simple recuperator cycle; sCO₂, Supercritical carbon dioxide; TIT, Turbine inlet temperature.

^{*} Corresponding author.

E-mail address: asleiti@qu.edu.qa (A.K. Sleiti).

<https://doi.org/10.1016/j.fuel.2021.120557>

Received 7 January 2021; Received in revised form 16 February 2021; Accepted 24 February 2021

Available online 8 March 2021

0016-2361/© 2021 The Author(s). Published by Elsevier Ltd. This is an open access article under the CC BY license (<http://creativecommons.org/licenses/by/4.0/>).

Nomenclature	
Symbols	Description (Units)
$A_{o,i}$	Heat transfer area of segment i of the recuperator (m^2)
$C_{c,i}$	Heat capacity rate of the fluid in the cold stream at segment i of the recuperator ($kW/^\circ C$)
$C_{h,i}$	Heat capacity rate of the fluid in the hot stream at segment i of the recuperator ($kW/^\circ C$)
C_{min}	Minimum heat capacity rate of the fluid in the cold or hot stream at segment i of the recuperator ($kW/^\circ C$)
$CP_{avg,h,i}$	Average specific heat of the hot fluid across segment i of the recuperator ($kJ/kg\cdot^\circ C$)
$CP_{avg,c,i}$	Average specific heat of the cold fluid across segment i of the recuperator ($kJ/kg\cdot^\circ C$)
d	Diameter of the each recuperator channel (mm)
d_{eq}	Equivalent hydraulic diameter of the recuperator channel (mm)
$\dot{E}_{D,k}$	Exergy destruction rate of component k (kW)
$\dot{E}_{q,k}$	Exergy rate due to heat transfer of component k (kW)
$\dot{E}_{i,k}$	Exergy rate at the inlet of component k (kW)
$\dot{E}_{o,k}$	Exergy rate at the outlet of component k (kW)
$\dot{E}_{p,k}$	Exergy product of component k (kW)
$\dot{E}_{f,k}$	Exergy fuel of component k (kW)
$\dot{E}_{L,k}$	Exergy loss of to the environment of component k (kW)
$h_{c,i}$	Enthalpy at the inlet of the compressor (kJ/kg)
$h_{c,o}$	Actual enthalpy at the outlet of the compressor (kJ/kg)
$h_{sc,o}$	Isentropic enthalpy at the outlet of the compressor (kJ/kg)
$h_{co,i}$	Enthalpy at the combustor inlet (kJ/kg)
$h_{t,i}$	Enthalpy at the inlet of the turbine (kJ/kg)
$h_{t,o}$	Actual enthalpy at the outlet of the turbine (kJ/kg)
$h_{st,o}$	Isentropic enthalpy at the outlet of the turbine (kJ/kg)
$h_{ht,i}$	Heat transfer coefficient of the hot fluid in the hot stream at segment i ($kW/m^2\cdot^\circ C$)
$h_{cd,i}$	Heat transfer coefficient of the cold fluid in the hot stream at segment i ($kW/m^2\cdot^\circ C$)
k_p	Thermal conductivity of the plate of the recuperator material ($kW/m^2\cdot^\circ C$)
l_i	Length of each segment of the heat exchanger (mm)
\dot{m}_{CO_2}	Mass flow rate of the CO_2 (kg/s)
\dot{m}_{H_2O}	Mass flow rate of the water vapor (kg/s)
\dot{m}_{O_2}	Mass flow rate of O_2 (kg/s)
\dot{m}_{CH_4}	Mass flow rate of the fuel (Methane, CH_4) (kg/s)
\dot{m}_{rCO_2}	Mass flow rate of the recycled CO_2 (kg/s)
Nu_i	Nusselt number of the fluid through cold/hot segment i of the recuperator
N_{pair}	Number of the hot/cold channel pairs of the recuperator
$P_{t,i}$	Pressure at the inlet of the turbine (MPa)
$P_{t,o}$	Pressure at the outlet of the turbine (MPa)
$P_{c,i}$	Pressure at the inlet of the compressor (MPa)
$P_{c,o}$	Pressure at the outlet of the compressor (MPa)
Pr_i	Prandtl number of the fluid through cold/hot segment i of the recuperator
P_{net}	Net power produced by the power cycle (MW)
Q_i	Heat transfer from the hot to the cold fluid of the recuperator at segment i (kW)
Re_i	Reynolds number of the fluid through cold/hot segment i of the recuperator
$T_{t,i}$	Temperature at the inlet of the turbine ($^\circ C$)
$T_{t,o}$	Temperature at the outlet of the turbine outlet ($^\circ C$)
$T_{c,i}$	Temperature at The inlet of the compressor ($^\circ C$)
$T_{c,o}$	Temperature at the outlet of the compressor ($^\circ C$)
$T_{co,i}$	Temperature of the recycled CO_2 at the combustor inlet ($^\circ C$)
T_{hi}	Temperature of the hot fluid at the inlet of segment i ($^\circ C$)
T_{hi+1}	Temperature of the hot fluid at the outlet of segment i ($^\circ C$)
T_{ci}	Temperature of the cold fluid at the inlet of segment i ($^\circ C$)
T_{ci+1}	Temperature of the cold fluid at the outlet of segment i ($^\circ C$)
t_p	Thickness of each channel of the recuperator (mm)
$\dot{W}_{t,a}$	Actual power produced by the turbine (kW)
$\dot{W}_{c,a}$	Actual power consumed by the compressor (kW)
Greeks letters	
δ_{rel}	Relative roughness
f_i	Friction factor at segment i
μ_i	Viscosity of the fluid at average temperature across segment i (kg/m-s)
η_c	Isentropic efficiency of the compressor
η_t	Isentropic efficiency of the turbine
η_g	Conversion efficiency of the generator
η_{th}	Thermal efficiency of the cycle (%)
ρ_i	Density of the fluid at average temperature across segment i (kg/m^3)
ϵ_k	Second-law efficiency of component i (%)
ϵ_r	Effectiveness of the recuperator (%)

Brayton cycle, the performance of the sCO_2 cycle can be enhanced by incorporating preheating and reheating [26] multi-expansion [27] and intercooling compression processes [28]. However, the common shortcoming of these processes is the addition of a new component or more to the layout, which increases the capital and maintenance costs and adds more complexity.

Up to now, fossil fuels are the major resource of worldwide energy [23] that produce combustion by-products (mainly CO_2) resulting in environmental pollution and greenhouse effects [29,30]. So, sCO_2 power technologies with minimum or no emissions suggests a viable solution for this issue. One of these technologies is the Allam cycle [24,25] developed by 8 Rivers Capital company and combines oxy-fuel combustion sCO_2 power cycle. Its major advantages are its ability to capture the produced CO_2 from the oxy-combustion process and its high power efficiency and specific work. To investigate its feasibility and to prove the design and operation of the whole cycle, a demonstration plant is built in La Port, Texas with 50 MWth natural gas fuel input [31]. Heatrec Company develops the high recuperative heat exchangers of this

plant, while Toshiba provides its turbine and combustor. Other oxy-combustion cycles with different configurations and are able to capture the produced CO_2 can be found in [32–37]. The quasi-combined and the recuperated Cryogenic Pressurized Oxy-Combustion (CPOC) cycles have thermal efficiencies of 65.6% and 63%, respectively [35]. Even though these cycles have very high efficiencies, they are impractical cycles due to their layout complexity, high turbine inlet temperature (TIT), and cryogenic cooling system. The efficiency of the CPOC cycle without recuperator and with moderate TIT is about 30% with a simpler layout [35]. The basic Allam cycle that is without reheating process and the Allam cycle with reheating process have efficiencies (at the same design conditions) of about 59% and 60%, respectively [38]. In contrast to the conventional sCO_2 closed loop power cycles, the working fluid of the cycles driven by a direct oxy-fuel combustor (such as Allam cycle) is not pure CO_2 . It includes other impurities such as water vapor (the most significant) and other residual components from the combusted fuel (e.g. H_2S , N_2 , etc.) [31]. This imposes the addition of a water vapor separator to these configurations. Furthermore, there is a by-

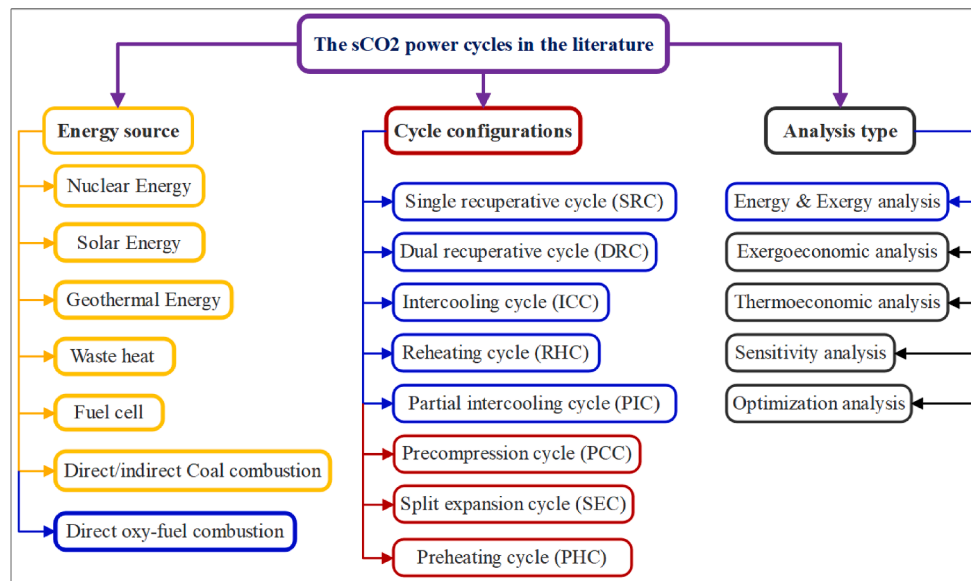


Fig. 1. Heat sources, cycle configurations, and analyses of the $s\text{CO}_2$ power cycles in the literature.

product CO_2 that results from the combustion, which must be exported to maintain constant flow rates through the cycle components. Since these cycles work at supercritical conditions, the exported CO_2 could be transformed for commercialized applications or to storage sinks by offshore pipelines that are designed for CO_2 transportations.

Thermodynamics energy and exergy analyses are necessary to obtain efficient and cost-effective design and operation of energy systems. Exergy analysis is used to control energy losses by determining the major contributors to exergy destruction and potential readjustments in the power cycle processes to improve the overall efficiency. Furthermore, exergy analysis helps categorizing exergy losses into avoidable and unavoidable types to identify practical improvements. This kind of analysis is a fundamental step to compare various configurations of the proposed in this study innovative oxy-combustion $s\text{CO}_2$ power cycles before conducting advanced economic evaluations. Exergy analysis is being used in other energy systems such as aircraft engines [39–42], coal-fired cycles [43–45], electric vehicles [46,47], waste heat recovery systems [48,49], combined cycles with solar [50–54], and geothermal sources [14,55] or combined with Kalina cycles [10,56], Miller cycle [57] organic Rankine cycles [58,59], fuel cell systems [60] and other applications [61,62]. However, exergy analysis studies for oxy-combustion $s\text{CO}_2$ power cycles are still limited to the basic Allam cycle in open literature and need to be extended to other innovative cycle configurations, which is one of the main objectives and contributions of the present study.

In 2016, Penkuhn and Tsatsaronis [63] have performed an exergy analysis of the Allam cycle and compared it with similar oxy-combustion cycles. They have concluded that The efficiencies of the main system components of the Allam cycle (such as combustor, turbine and CO_2) recompression are similar to those of the similar cycles. However, they have recommended for further advanced exergy analysis frameworks to quantify the potentials for the improvement of the Allam cycle components. Scaccabarozzi et al. [24] performed in-depth thermodynamic analysis and numerical optimization for the Allam cycle arriving at some optimized operating conditions for maximizing the cycle energy efficiency and recommended further techno-economic optimization for future work. In 2019, Rogalev et al. [64] performed equipment development study alongside thermodynamic optimization for Allam cycle. They stressed that oxygen purity should not be higher than 91% to minimize the power consumed by the ASU and they proposed a single flow, double casing construction for the developed $s\text{CO}_2$ gas turbine. Also, in 2019, Hervas and Petrakopoulou [65] have introduced an

exergoeconomic analysis of the Allam cycle at the design point of the original developers [66] without investigation for the effects of the major operating conditions. Recently, in 2020, Chan et al. [67] introduced a novel layout of the Allam cycle by integrating a reheating system to the original Allam cycle. Based on their energetic, exergetic, and optimization analysis, they found that the thermal efficiency of the novel cycle is lower than that of the original Allam cycle, however the net power output of their cycle is about 2.2 times higher.

As discussed above, several cycle configurations of the $s\text{CO}_2$ power cycles are proposed in the literature, which are summarized in Fig. 1. Many researchers have investigated the performance of configurations that are integrated with one of the energy sources shown in Fig. 1 (nuclear, solar, geothermal, waste heat and coal) [1,68] except for the direct oxy-combustion. Examples of analyses of these configurations in terms of energy, exergy, exergoeconomic, thermo-economic, sensitivity, and optimization can be found in [12,28,69–76].

However, investigations of integrating direct oxy-fuel combustion (the last energy source in Fig. 1) with $s\text{CO}_2$ power cycle are limited in open literature. Only few studies have investigated the energy [67,77,78] and exergy [63] performances of Allam cycle (that is powered by a direct oxy-combustor). However, these studies considered only high turbine inlet temperatures (above 1150°C) at high pressures (20 MPa to 30 MPa), which require special design for the turbine (such as the need for a coolant fluid to cool the turbine and improved design for the turbine blades [66]) to withstand these conditions. Furthermore, the high turbine inlet temperature dictates high operating temperatures for the recuperators; 700°C to 750°C at high pressures, which makes their design quit challenging [24]. In addition, these conditions increase the capital costs of the cycle components. For these reasons, the present study investigates the performance of various oxy-combustion $s\text{CO}_2$ power cycles at moderate turbine inlet temperatures (550°C to 750°C), which is also a practical range for the $s\text{CO}_2$ power cycles to be integrated with other energy sources such as solar energy, nuclear energy and waste heat. Moreover, thorough energy and exergy models for the $s\text{CO}_2$ power cycle configurations that are driven by the direct oxy-fuel combustor are not available in the literature.

The present study addresses the above research gaps in systematic and comprehensive way including the shortcomings due to adding extra components, the high operating temperatures and the lack of studies on using direct oxy-combustion for $s\text{CO}_2$ power cycles. Compared to the other research studies (such as [71,79–81]), the main novelty aspects and contributions of the of the present study include:

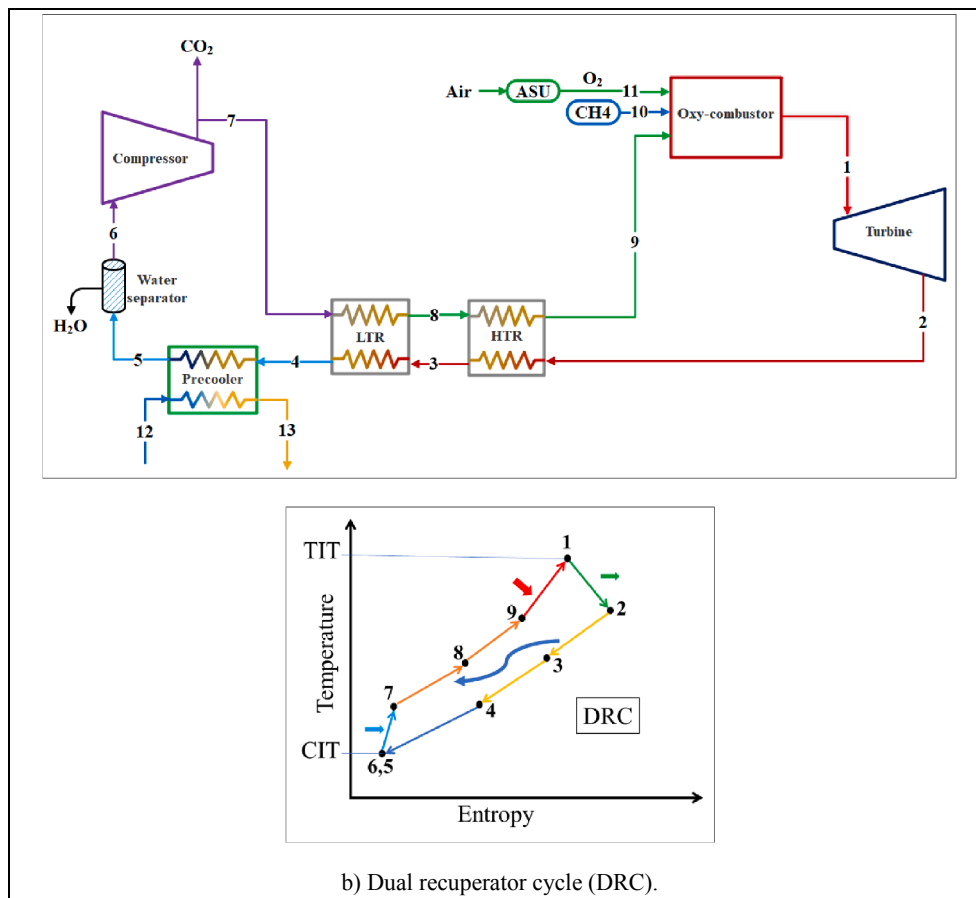


Fig. 2. (continued).

Table 1, however they have limitations (also listed in Table 1) that will be investigated as well.

Starting with the simple recuperative cycle configuration (SRC), Fig. 2 (a), it consists of the basic components of a typical Brayton cycle including the compressor, recuperator, combustor, turbine, and pre-cooler in addition to the water-separator, which is a special component for the direct oxy-fuel sCO₂ cycles. The SRC is selected as a reference configuration in this study to explain the thermodynamic energy and exergy models. In the SRC, the combustion products (CO₂ and water vapour) enter the turbine at high pressure and temperature (state 1) to expand and drive the electric generator and the compressor of the cycle. These products leave the turbine with relatively high temperature (2); pass through the recuperator to preheat the recycled sCO₂ before entering the combustor (7). Leaving the recuperator, the combustion products are cooled further in the pre-cooler to a temperature that is appropriate for effective work of the compressor (4). The water vapor is separated from the combustion products (process 4–5) and the highly pure CO₂ is then compressed by the compressor (process 5–6). A small fraction of the compressed sCO₂ must be exported to maintain the mass flow rate balance through the cycle. Then, the recycled sCO₂ is preheated in the recuperator (process 6–7) and enters the combustor with the fuel (state 8) and oxygen (state 9). The recycled sCO₂ dilutes the temperature of the combustion process to the desired inlet temperature of the turbine; then the cycle is repeated.

The dual recuperative cycle (Fig. 2 (b)) utilizes two recuperators (high and low-temperature recuperators) to recover more heat from the combustion products leaving the turbine. The compression process could be applied with an intercooling process to reduce the power consumed by the compressors as shown in the intercooling cycle ICC (Fig. 2 (c)). In the ICC, compressor 1 raises the pressure of the sCO₂ from

the lower cycle pressure to an intermediate value. Then the sCO₂ is cooled by an intermediate cooler with constant pressure to the desired temperature at the inlet of compressor 2, which compresses it to the higher pressure of the cycle. In addition to that, a partial intercooling cycle (PIC) is also investigated in this study. It is similar to the ICC with the splitting of the sCO₂ into two streams after leaving compressor 1 as shown in (Fig. 2 (e)). One stream passes through an intermediate cooler and is compressed to the higher pressure. The other stream is compressed by compressor 3 to the high pressure (without intercooling). Furthermore, the reheating cycle (RHC) is also presented in this study as shown in (Fig. 2 (d)), where the reheater is placed between turbine 1 and turbine 2.

3. System thermodynamic model

In this section, the thermodynamic energy and exergy models of each component of the studied configurations are introduced. The following assumptions were made for the cycle calculations:

- Steady-state analysis.
- Pressure losses in tubes are ignored.
- The variations of the kinetic and potential energies across each component are neglected.
- The heat losses from the components to the ambient are neglected.

3.1. Energy model of the system

The components of the studied configurations can be divided into four major types; compressors, combustors, turbines, and heat

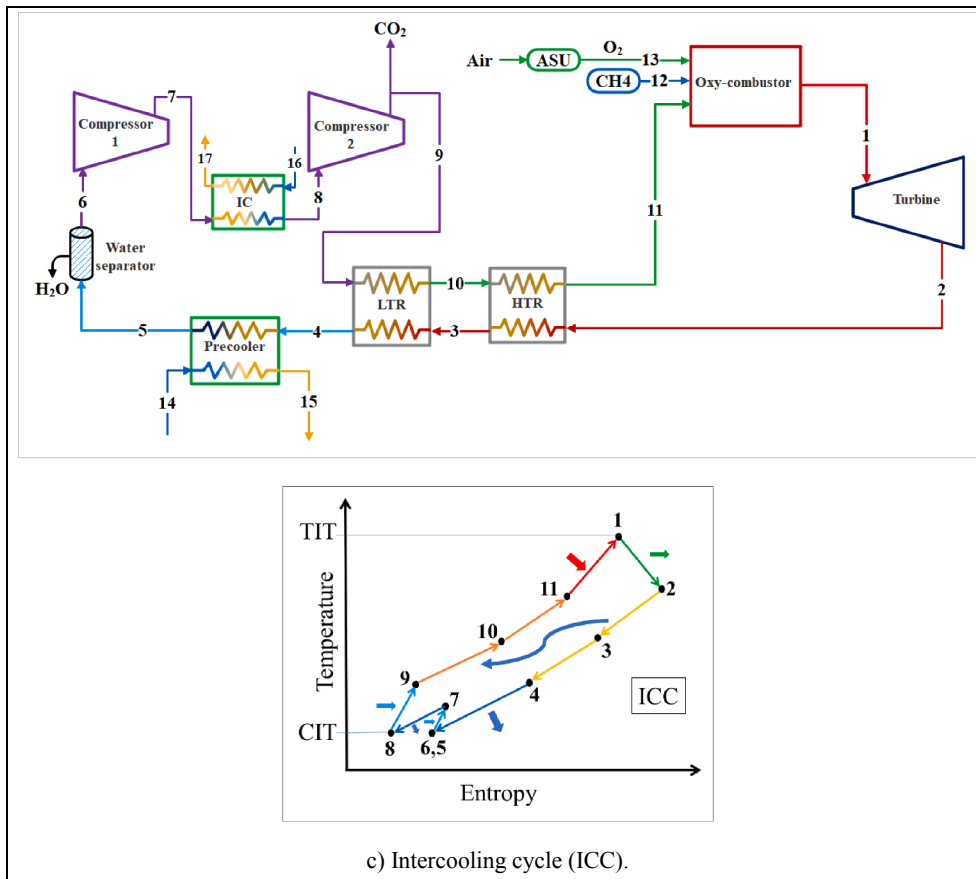


Fig. 2. (continued).

exchangers including the recuperators, pre-cooler, and intercooler. In the next subsections, the energy model of each type is introduced.

3.1.1. Compressor

The parameters of the compressor at its inlet and outlet are presented in Fig. 3. The actual work consumed by the compressor is given as:

$$\dot{W}_{c,a} = \dot{m}_{CO_2} [h_{sc,o} - h_{c,i}]_{CO_2} / \eta_c \quad (1)$$

where η_c is the isentropic efficiency of the compressor, $h_{c,i}$ is the enthalpy at the compressor inlet and $h_{sc,o}$ is the isentropic enthalpy at the outlet of the compressor. The actual outlet temperature of the compressor could be obtained by the actual enthalpy and the outlet pressure using the definition of the isentropic efficiency, which is given as [84]:

$$\eta_c = \frac{h_{sc,o} - h_{c,i}}{h_{c,o} - h_{c,i}} \quad (2)$$

3.1.2. Combustor

The reactants and combustion products of the oxy-combustor are shown in Fig. 4. The fuel (assumed to be pure methane) is combusted with the oxygen (provided by the air-separation unit ASU) and the recycled sCO₂ to produce the CO₂ and water vapor at the desired temperature of the turbine. The actual combustion formula is given as:



The mass balance at the inlet and outlet of the oxy-combustor is given as:

$$\dot{m}_{O_2} + \dot{m}_{CH_4} + \dot{m}_{rCO_2} = \dot{m}_{CO_2} + \dot{m}_{H_2O} \quad (4)$$

And the energy balance is given as:

$$\begin{aligned} \dot{m}_{O_2} [h_{co,i}]_{O_2} + \dot{m}_{CH_4} [h_{co,i}]_{CH_4} + \dot{m}_{rCO_2} [h_{co,i}]_{CO_2}, \\ = \dot{m}_{CO_2} [h_{co,o}]_{CO_2} + \dot{m}_{H_2O} [h_{co,o}]_{H_2O} \end{aligned} \quad (5)$$

From Eq. (3), it can be concluded that:

$$\dot{m}_{O_2} = 4\dot{m}_{CH_4} \quad (6)$$

$$\dot{m}_{rCO_2} = \dot{m}_{CO_2} - 2.77\dot{m}_{CH_4} \quad (7)$$

3.1.3. Turbine

Referring to the parameters of the turbine shown in Fig. 5, the designed power capacity of the cycle is given as [84]:

$$P_{net} = \frac{\dot{W}_{t,a} - \dot{W}_{c,a}}{\eta_g} \quad (8)$$

where,

$$\dot{W}_{t,a} = \eta_t \times \{ \dot{m}_{CO_2} [h_{t,i} - h_{st,o}]_{CO_2} + \dot{m}_{H_2O} [h_{t,i} - h_{st,o}]_{H_2O} \} \quad (9)$$

where η_t is the isentropic efficiency of the turbine and it is given as:

$$\eta_t = \frac{h_{t,o} - h_{t,i}}{h_{st,o} - h_{t,i}} \quad (10)$$

The thermal efficiency of the cycle is given as:

$$\eta_{th} = \frac{P_{net}}{\dot{m}_{CH_4} \times LHV} \quad (11)$$

3.1.4. Recuperators, Precooler, and intercooler model

There are two types of heat exchangers used in the studied configurations. One is the recuperator that is used to recover heat from the combustion products to heat the recycled sCO₂. The other one is the pre-

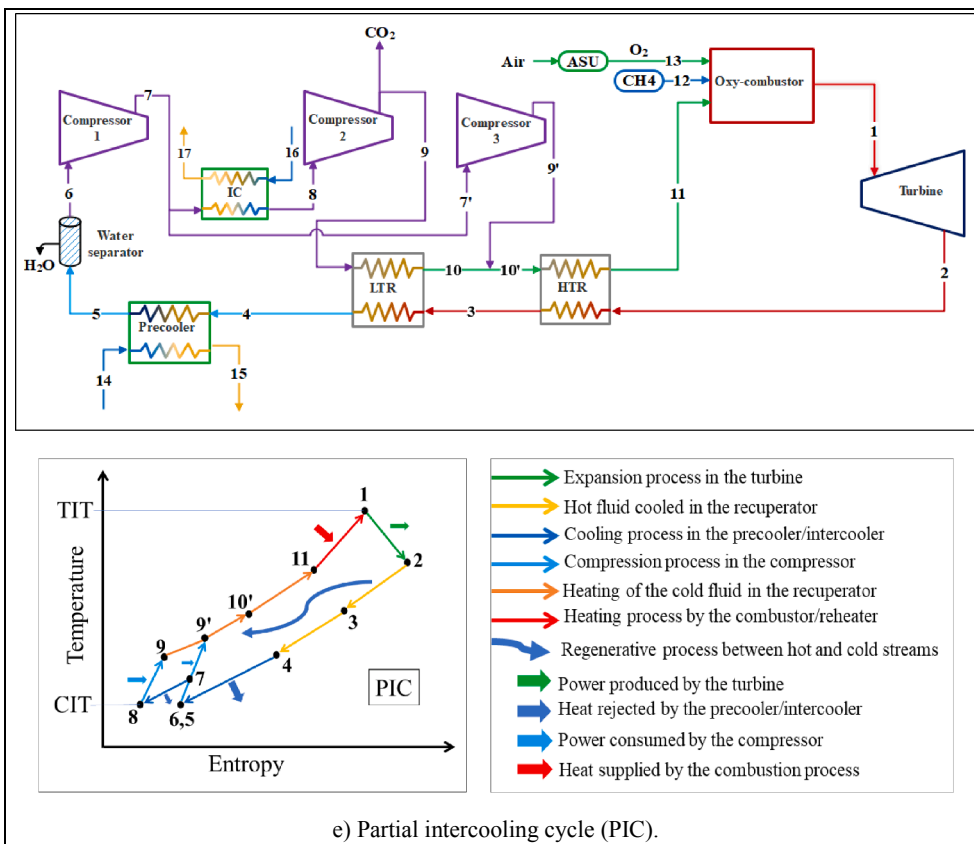
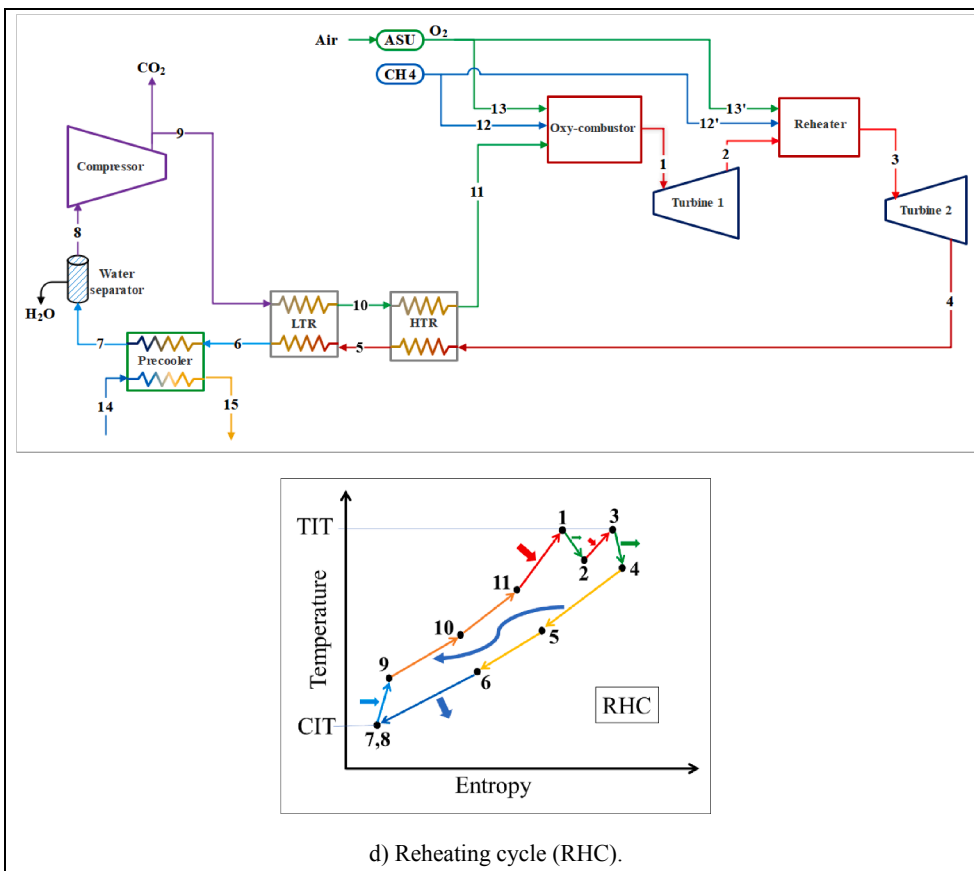


Fig. 2. (continued).

Table 1

Features and limitations of the five cycle configurations proposed in this study [71,79,82,83].

Cycle	Features	Limitations
SRC	<ul style="list-style-type: none"> - Simple configuration. - Lower capital and operational costs. 	<ul style="list-style-type: none"> - Limited efficiency by the temperature pinch-point problem in the recuperator.
DRC	<ul style="list-style-type: none"> - Minimizes the pinch-point problem. - Recovers more heat with reasonable size for each recuperator. - Reduces the load of the precooler 	<ul style="list-style-type: none"> - Still have pinch-point problem within the LTR which relatively limits its efficiency. - Higher capital cost than the SRC.
ICC	<ul style="list-style-type: none"> - Minimizes the compression power - Achieves the highest efficiency among the other configurations. 	<ul style="list-style-type: none"> - Higher capital cost due to the addition of second compressor and the intercooler.
RHC	<ul style="list-style-type: none"> - Produces larger output power than other configurations. 	<ul style="list-style-type: none"> - Higher capital and operational costs due to the addition of a reheater and second turbine
PIC	<ul style="list-style-type: none"> - Eliminates the pinch-point problem of the LTR. 	<ul style="list-style-type: none"> - Higher capital and operational costs (3 compressors and intercooler are needed). - More complex structure.

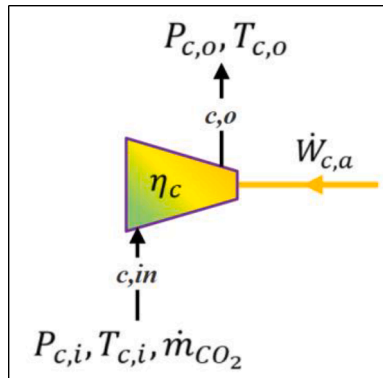


Fig. 3. Schematic model of the compressor.

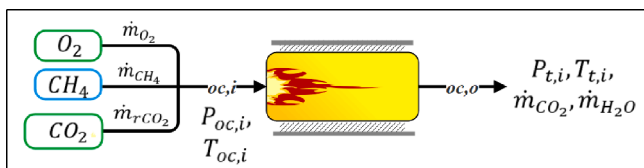


Fig. 4. Schematic model of the combustion chamber.

cooler (and intercooler) which is used to cool the combustion products to the desired compressor inlet temperature using dry (air) or wet (water) cooling process. Due to its compactness and high effectiveness, the printed circuit heat exchanger (PCHE) is selected for the sCO₂ power cycles [85,86]. It consists of alternately cold and hot flow channels as shown in Fig. 6 (a) and (b). The specifications of the PCHE used in this study are presented in Table 2. Since the physical properties of the sCO₂ change dramatically near critical and quasi-critical points, it is necessary to discretize the heat exchanger unit into several segments (m) along the flow direction to obtain accurate output from the performed calculations, Fig. 6. Assuming uniform flow, a single pair of the channels can be modeled as a heat exchanger and the heat transfer across each segment is given as:

$$Q_i = U_{o,i} A_{o,i} \Delta T_i \quad (12)$$

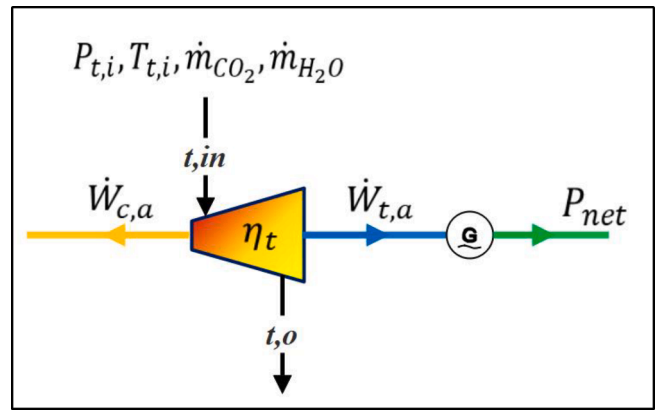


Fig. 5. Schematic model of the turbine.

where $U_{o,i}$ is the overall heat transfer coefficient of each segment, $A_{o,i}$ is the heat transfer area between the hot and cold channel, and ΔT_i is the logarithmic mean temperature difference (LMTD) across each segment which is expressed as:

$$\Delta T_i = \frac{(T_{h,i+1} - T_{c,i+1}) - (T_{h,i} - T_{c,i})}{\ln\left(\frac{T_{h,i+1} - T_{c,i+1}}{T_{h,i} - T_{c,i}}\right)} \quad (13)$$

and $U_{o,i}$ is given as:

$$U_{o,i} = \frac{1}{\frac{1}{h_{h,i}} + \frac{1}{h_{c,i}} + \frac{t_p}{k_p}} \quad (14)$$

where $h_{h,i}$ and $h_{c,i}$ is the heat transfer coefficients between the hot and cold flow and the plate in each channel pair, respectively. For turbulent flow, these coefficients are obtained from the Gnielinski empirical Nusselt number correlation as recommended by Hesselegraves et al. [87] and verified by Serrano et al. [88] for the straight semi-circular channels, which is given as:

$$Nu_i = \frac{\left(\frac{f_c}{8}\right) (Re_i - 1000) \cdot Pr_i}{1 + 12.7 \cdot (Pr_i^{2/3} - 1) \cdot \sqrt{f_{c,i}/8}}, \quad 5000 \leq Re \leq 5 \times 10^6, \quad Pr = 0.5 \text{ to } 2000 \quad (15)$$

$$f_{c,i} = \left(\frac{1}{1.8 \log Re_i - 1.5}\right)^2 \quad (16)$$

$$Re_i = \frac{4\dot{m}_i}{\pi \mu_i d_{eq}} \quad (17)$$

where d_{eq} is the equivalent hydraulic diameter of the semi-circular channel which is:

$$d_{eq} = \frac{4\pi d^2}{8 \cdot \left(\frac{\pi}{2} d + d\right)} \quad (18)$$

The mass flow rate (\dot{m}) in each hot and cold channel is given as:

$$\dot{m}_{h,i} = \frac{\dot{m}_{hot}}{N_{pairs}}, \quad \dot{m}_{c,i} = \frac{\dot{m}_{cold}}{N_{pairs}} \quad (19)$$

The number of the hot-cold channel pairs was selected such that the total pressure drop does not exceed the given percentage in Table 2. The total pressure drop (in hot or cold sides) is given as follows:

$$\Delta P_{total} = N_{pairs} \sum \Delta P_i \quad (20)$$

$$\Delta P_i = f_i \cdot \frac{l_i}{d_{eq}} \cdot \rho_i \cdot \frac{V_i^2}{2} \quad (21)$$

where f_i is the friction factor. For turbulent flow, it is given as:

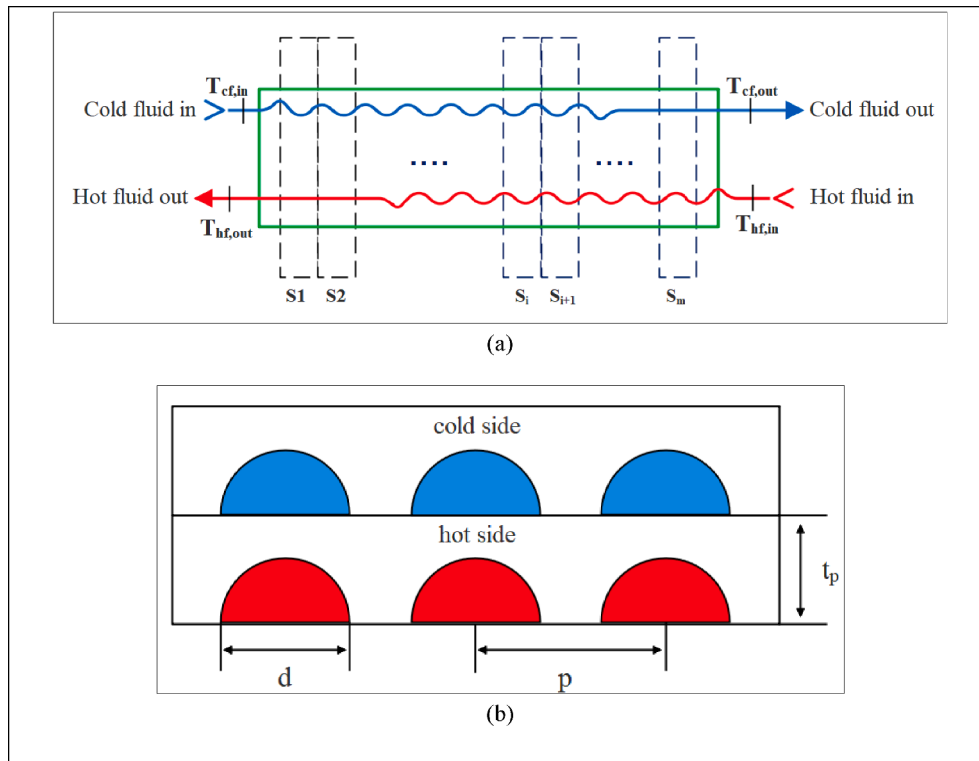


Fig. 6. Schematic model of the (a) heat exchanger segments, (b) cross-section of one layer of the PCHE.

Table 2
Specifications of the PCHE [71].

PCHE	
Material	stainless steel 304
Channel diameter	2 mm
Plate thickness	1.5 mm
pitch of channel	2.4 mm
Coefficient of thermal conductivity	19 W/m·°C
sCO ₂ side allowable pressure drop	5%

$$f_i = 0.11 \cdot (\delta_{rel} + 68 \cdot (441.19 \delta_{rel}^{-1.1772})^{-1})^{0.25} \quad (22)$$

δ_{rel} is the relative roughness given as:

$$\delta_{rel} = e/d \quad (23)$$

The length of each segment l_i is obtained from the definition of the surface area of each segment $A_{o,i} = \pi \cdot d \cdot l_i$, which is calculated from Eq. (12). To solve Eq. (12) for l_i , the heat transfer across each segment is substituted in terms of the temperature difference of the hot and cold stream as follows:

$$Q_i = \dot{m}_{h,i} \cdot c_{p,avg,h,i} \cdot \Delta T_{h,i}, \quad \Delta T_{h,i} = T_{h,i+1} - T_{h,i} \quad (24)$$

$$Q_i = \dot{m}_{c,i} \cdot c_{p,avg,c,i} \cdot \Delta T_{c,i}, \quad \Delta T_{c,i} = T_{c,i+1} - T_{c,i} \quad (25)$$

The temperature at the exit of each cold segment is obtained by the definition of the heat exchanger (recuperator) effectiveness as:

$$\epsilon_r = \frac{\dot{m}_{h,i} (T_{h,i+1} - T_{h,i})}{C_{min} (T_{h,i+1} - T_{c,i})} \quad (26)$$

$$C_{min} = \min(C_{h,i}, C_{c,i}) \quad (27)$$

$$C_{h,i} = \dot{m}_{h,i} c_{p,avg,h,i}, \quad C_{c,i} = \dot{m}_{c,i} c_{p,avg,c,i} \quad (28)$$

The above approach is clearly justified as shown in Fig. 6, where the

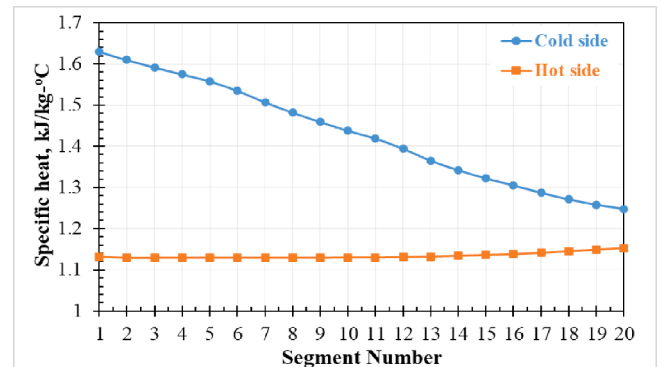


Fig. 7. Variation of the sCO₂ specific heat at each cold and hot segment of the recuperator. This figure is generated at: $T_{hot,1} = 400$ °C, $T_{hot,20} = 200$ °C, $P_{hot} = 8$ MPa & $T_{cold,1} = 150$ °C, $T_{cold,20} = 350$ °C, $P_{cold} = 20$ MPa. Total of 20 equally spaced segments are used.

CO₂ specific heat (C_p) of the cold side of the recuperator is changing significantly from the inlet to the outlet. The change in C_p of the hot side shown in Fig. 7, although less than the cold side, is also important to include in the calculations to improve the accuracy of the results.

3.2. Exergy model of the system

After obtaining the temperature and pressure at each state point from the energy model, the exergy balance for component k is used to obtain its exergy destruction rate $\dot{E}_{D,k}$, which is given as [89]:

$$\dot{E}_{D,k} = \sum_j \dot{E}_{q,k} + \dot{W}_k + \sum_i \dot{E}_{i,k} - \sum_o \dot{E}_{o,k} \quad (29)$$

The exergy destruction rate is used to obtain the real thermodynamic efficiency of component k in terms of its fuel exergy ($\dot{E}_{F,k}$) and product exergy ($\dot{E}_{P,k}$) or in terms of exergy destruction ($\dot{E}_{D,k}$) and product exergy

Table 3
Definitions of fuel, product, destruction, and loss exergies for the components of the SRC.

Component	$\dot{E}_{F,k}$	$\dot{E}_{P,k}$	$\dot{E}_{D,k}$	$\dot{E}_{L,k}$
Oxy-combustor	$\dot{E}_7 + \dot{E}_8 + \dot{E}_9$	\dot{E}_1	$\dot{E}_7 + \dot{E}_8 + \dot{E}_9 - \dot{E}_1$	0
Turbine	$\dot{E}_1 - \dot{E}_2$	$\dot{W}_{t,a}$	$\dot{E}_1 - \dot{E}_2 - \dot{W}_{t,a}$	0
Compressor	$\dot{W}_{c,a}$	$\dot{E}_6 - \dot{E}_5$	$\dot{W}_{c,a} - (\dot{E}_6 - \dot{E}_5)$	0
Recuperator	$\dot{E}_2 - \dot{E}_3$	$\dot{E}_7 - \dot{E}_6$	$\dot{E}_2 - \dot{E}_3 - (\dot{E}_7 - \dot{E}_6)$	0
Precooler	\dot{E}_3	\dot{E}_4	$\dot{E}_3 - \dot{E}_4 - (\dot{E}_{11} - \dot{E}_{10})$	$\dot{E}_{11} - \dot{E}_{10}$

Table 4
Input parameters of the system.

Parameter	Range (Design value)
Desired output power, P_{net} MW	50
High pressure of the cycle, $P_{c,o}$ MPa	20–30 (20)
Pressure ratio, $r_c = \frac{P_{c,o}}{P_{c,i}}$	2–6 (2.56)
Intermediate pressure ratio, RPR	0.3–1(0.43)
Turbine inlet temperature, $T_{t,i}$ °C	550–750
Compressor inlet temperature, $T_{c,i}$ °C	35 – 50 (50)
Isentropic efficiency of the turbine, η_t [71]	90
Isentropic efficiency of the compressor, η_c % [90]	85
Effectiveness of the recuperators, ϵ_r % [71]	86
Efficiency of the generator, η_g % [91]	95
Lower heating value of the fuel, LHV kJ/kg [92]	50,050
Minimum LMTD across each heat exchanger segment, °C	2.5
Maximum LMTD across each heat exchanger segment, °C	15
Minimum temperature difference at the cold end of the recuperator (or LTR), °C	5
Maximum temperature difference at the hot end of the recuperator (or HTR), °C	60
Pressure drops across the combustor	3%

($\dot{E}_{P,k}$) as:

$$\epsilon_k = \frac{\dot{E}_{P,k}}{\dot{E}_{F,k}} = 1 - \frac{\dot{E}_{D,k}}{\dot{E}_{F,k}} \quad (30)$$

For the overall analysis of the system, the exergy loss to the environment ($\dot{E}_{L,k}$) must be considered such that the overall second law efficiency is:

$$\epsilon_o = \frac{\dot{E}_{P,k}}{\dot{E}_{F,k}} = 1 - \frac{\sum(\dot{E}_{D,k} + \dot{E}_{L,k})}{\sum \dot{E}_{F,k}} \quad (31)$$

Table 3 shows the definitions of $\dot{E}_{F,k}$, $\dot{E}_{P,k}$, $\dot{E}_{D,k}$, and $\dot{E}_{L,k}$ for the simple recuperative cycle (SRC) shown in Fig. 2 (a).

3.3. Solution procedures

To explain how to solve the numerical model of the recuperators, the solution procedures of the SRC are discussed in this section. The models presented by Equations (1) to (31) are coded and solved using Engineering Equation Solver (EES). The input parameters are listed in Table 4. Using Eq. (2) and Eq. (11), the temperatures at the outlet of the compressor and turbine are obtained, respectively. By specifying the required temperature difference at the hot end of the recuperator $\Delta T_{r,hot} = T_{t,o} - T_{co,i}$, the inlet temperature of the recycled sCO₂ to the combustor ($T_{co,i}$) is obtained. Then, Eqs. 1–11 are solved to obtain the mass flow rates and thermal efficiency. The numerical equations of the recuperator are solved to specify its size and the temperature at the inlet of the precooler. Since the temperatures at the inlet and outlet of the cold stream of the recuperators are known ($T_{c,o}$, $T_{co,i}$), and by assuming proper temperature difference in each cold segment ($\Delta T_{c,i}$) and estimating (N_{pairs}), Eqs. (19) and (25) are solved to obtain the amount of the heat transferred in each segment. Then, using Eqs. 26–28 (with a specific heat of the hot stream taken at the temperature $T_{h,i+1}$ for each segment), the temperature $T_{h,i}$ is calculated. Now, Eqs. 12–23 are solved and the resulting total pressure drop (in hot and cold streams) is obtained. If the pressure drops less than 5% of the pressure at the inlet of the stream, then the other energy and exergy calculations are performed. If not, the estimated N_{pairs} is edited until the pressure drop satisfies the allowable percent as shown by Fig. 8 that summarizes the solution procedures. The

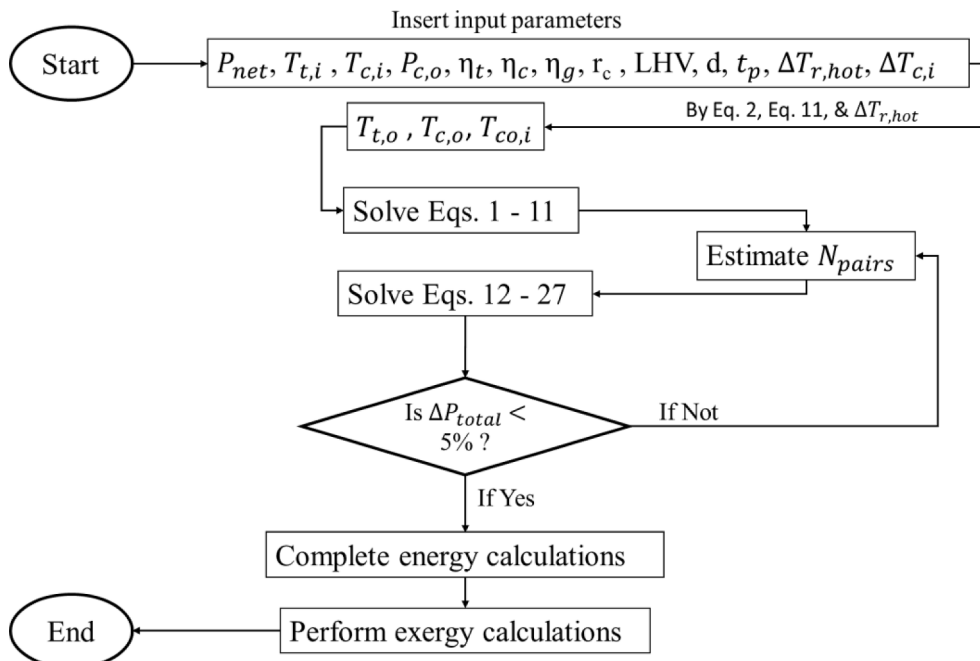


Fig. 8. Solution procedures of the SRC model.

Table 5
Comparison of the model results with data given by references [93] and [77].

Parameter	Ref. [93]	Present study	Ref. [77]	Present study
P_{net} , [MW]	393	393	401	401
\dot{m}_{CH_4} [kg/s]	15.5	14.6	15.5	14.58
\dot{m}_{O_2} [kg/s]	63	58.4	62	58.33
T_8 , [°C]	220	220	188	188
$P_{t,i}$, [bar]	300	300	300	300
$T_{t,i}$, [°C]	1150	1150	1150	1150
$P_{c,i}$, [bar]	30	30	30	30
T_2 , [°C]	795	777	780	770
T_3 , [°C]	63	72	77	69
T_7 , [°C]	738	717	723	692
T_6 , [°C]	79	52	26	49
Exported CO ₂ [kg/s]	55	42	42	43
\dot{m}_{rCO_2} [kg/s]	1264	1189	1200	1154
$\dot{W}_{t,a}$ [MW]	640	587	622	586
η_c , [-]	0.95	0.95	0.95	0.95
$\dot{W}_{c,a}$ [MW]	134	194	103	198
η_{th} [%]	50.78	48.50	51.8	49.55
Difference in efficiency (%)	4.5		4.3	

pressure drop was limited to a maximum of 5% to maintain the pressure ratio across the compressors and turbines near the optimized value of the thermal efficiency. Furthermore, based on other studies, it was found that the pressure drop across the recuperator channels does not exceed 5% for practical recuperators' sizes [24,67].

3.4. Validation of the model

The results obtained by the present model are validated by comparison with the data provided by Ricardo [93] and Haseli and Sifat [77] as shown in Table 5. Their results were reported for the Allam cycle configuration as shown in Fig. 9. It is composed from the same components as the SRC in this study except that the compression process in Allam cycle was performed using multi-stage intercooled compressors and pumps, while the SRC utilizes a single compression compressor. The operating conditions were adjusted to be identical with the operating conditions in [77] and [93] to validate the results of our own code.

It can be noted that the actual turbine work predicted by the present model is lower and the actual compressor work is higher than the provided data in these references. This difference is explained by that the

compression process in the present study is calculated as a single stage (without multi-inter cooling processes as done in [93;77]). Also, references [93] and [77] assumed that part of the heat generated by the air separation unit (ASU) is recovered by the recuperator, which enhances the thermal efficiency of the system. In these references, the details of the multi-inter cooling processes and the recovered heat were not provided to facilitate fair and complete comparison with the present study. However, the resulted difference does not exceed 4.5%. No other similar and suitable studies for comparison were found in open literature.

4. Results and discussion

In this section, the sensitivity of each configuration thermal efficiency to the variation of the main operating parameters (including pressure ratio (r_c), intermediate pressure ratio (RPR), turbine inlet temperature (TIT), and the compressor inlet temperature (CIT)) is simulated and discussed. Then, the exergy performance in terms of the second law efficiency is discussed.

Before proceeding to the discussion of the effects of the major operating conditions, it is important to give an insight on the significance of considering the variations in the CO₂ properties using the discretised model of the recuperators (Fig. 6). At the high-pressure cold stream side of the recuperators, the specific heat of the sCO₂ dramatically changes and when using its average value in the calculations, large errors occur in the outlet temperature from the HTR, and in the amount of the recycled sCO₂, which affects the other cycle calculations including the thermal efficiency, the pre-cooler loads, the gross power of the turbine and the compression power of the compressor. To demonstrate that,

Table 6
Comparison between the simulation results obtained by discretised-based calculations and average based calculations for the recuperators of the sCO₂ power cycle.

Parameter	Discretised-based results	Average-based results	Error (%)
$T_{co,i}$, [°C]	531.10	526.80	0.81
\dot{m}_{rCO_2} [kg/s]	367.50	406.1	-10.50
\dot{m}_{CH_4} [kg/s]	2.18	2.40	-10.09
\dot{m}_{O_2} [kg/s]	8.45	9.60	-13.61
$\dot{W}_{t,a}$ [MW]	71.98	78.62	-9.22
$\dot{W}_{c,a}$ [MW]	21.98	25.99	-18.20
Thermal efficiency, [%]	41.27	37.50	9.13

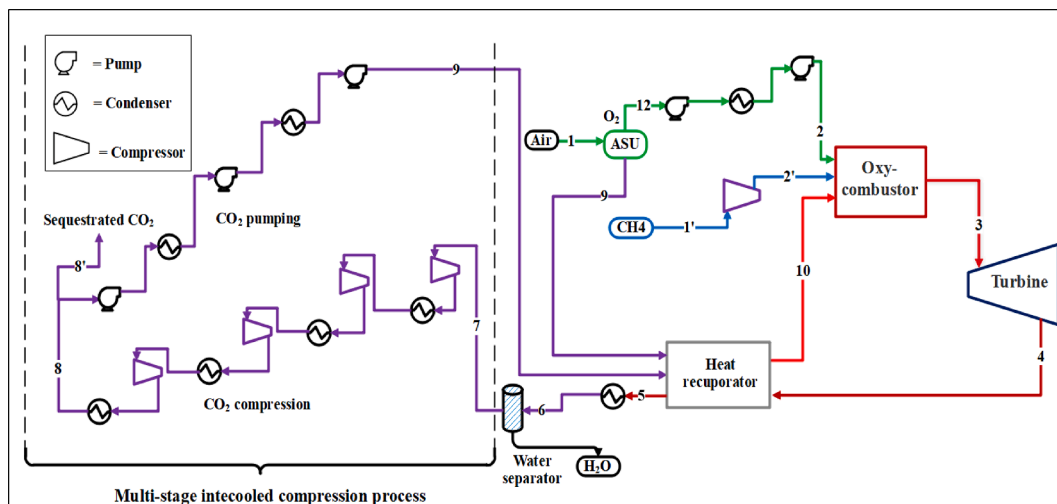


Fig. 9. Schematic diagram of the Allam cycle which analysed for the reported results in [77] and [93].

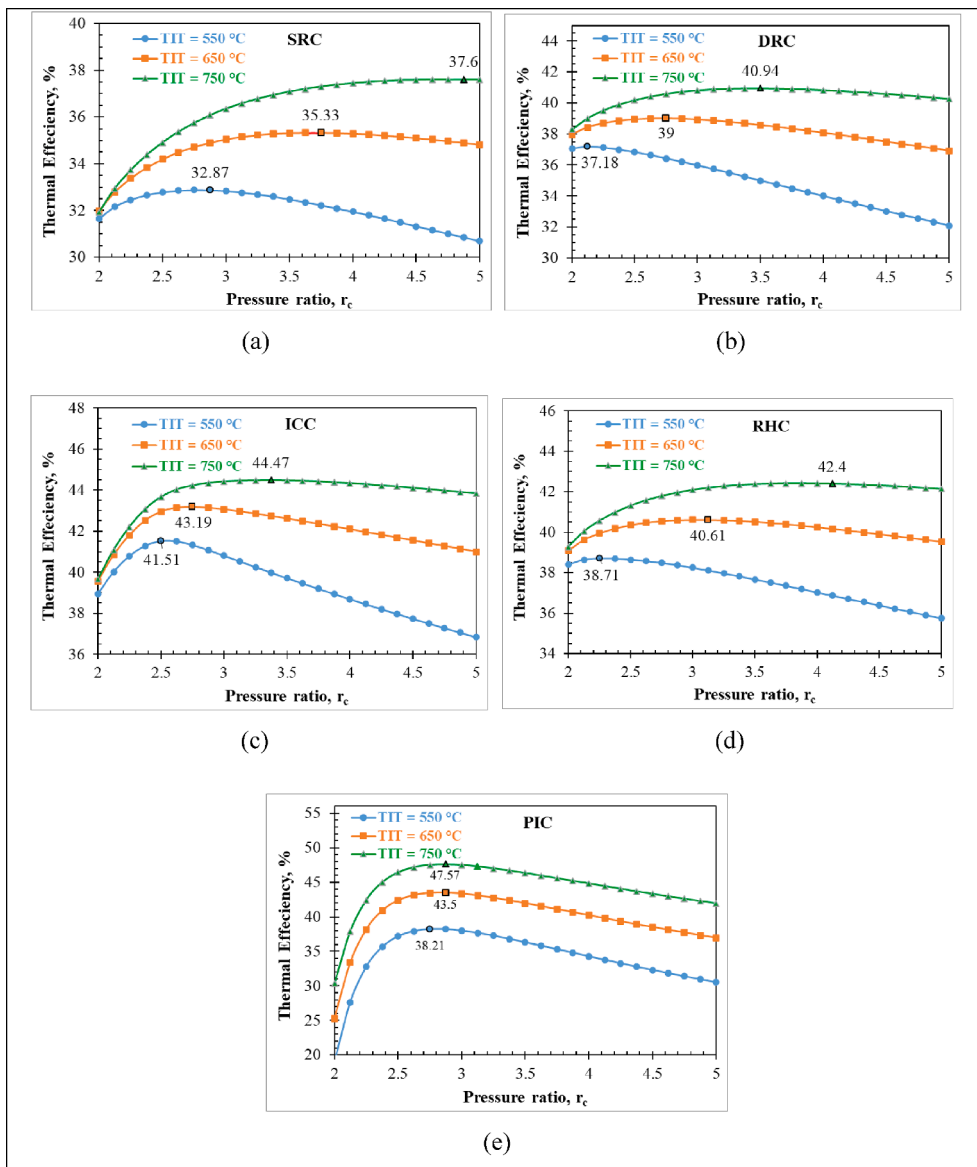


Fig. 10. Effect of the pressure ratio (r_c) on the thermal efficiency of the studied layouts at different inlet turbine temperatures. At $P_{c,o} = 20$ MPa, $T_{c,i} = 50$ °C, RPR = 0.3.

a comparison between the results obtained by the discretised model and by tacking the average specific heat across the recuperators is presented in Table 6. As shown in Table 6, unacceptable errors (9.13% in thermal efficiency) resulted from the average based calculations compared to the discretised based calculations. This confirms that the discretised model, which is applied in this study for sCO₂ power cycle recuperators is absolutely necessary to obtain accurate results. The error percentage in Table 6 is calculated as: (Discretised – Average) / Discretised.

4.1. Effect of the pressure ratio

Fig. 10 shows the effect of the pressure ratio on the thermal efficiency of the a) SRC, b) DRC, c) ICC, d) RHC, and e) PIC at different TITs and at fixed high-pressure of $P_{c,o} = 20$ MPa, fixed CIT of 50 °C, while the pressure ratio r_c changes from 2 to 5. From Fig. 10, it can be noted that at fixed TIT the thermal efficiency increases with the increase of the pressure ratio r_c until it reaches a maximum at an optimal pressure ratio then decreases with further increase in the r_c . This is explained by that higher r_c increases the expansion work of the turbine and the consumed work of the compressor. However, the increase of the work of the

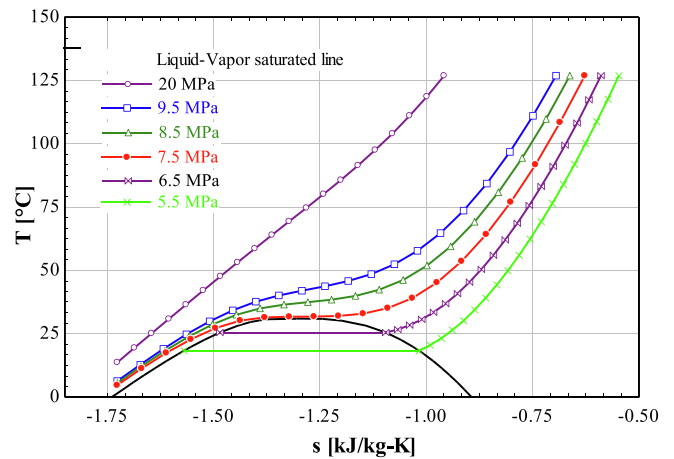


Fig. 11. T-s diagram of the CO₂ at various pressures.

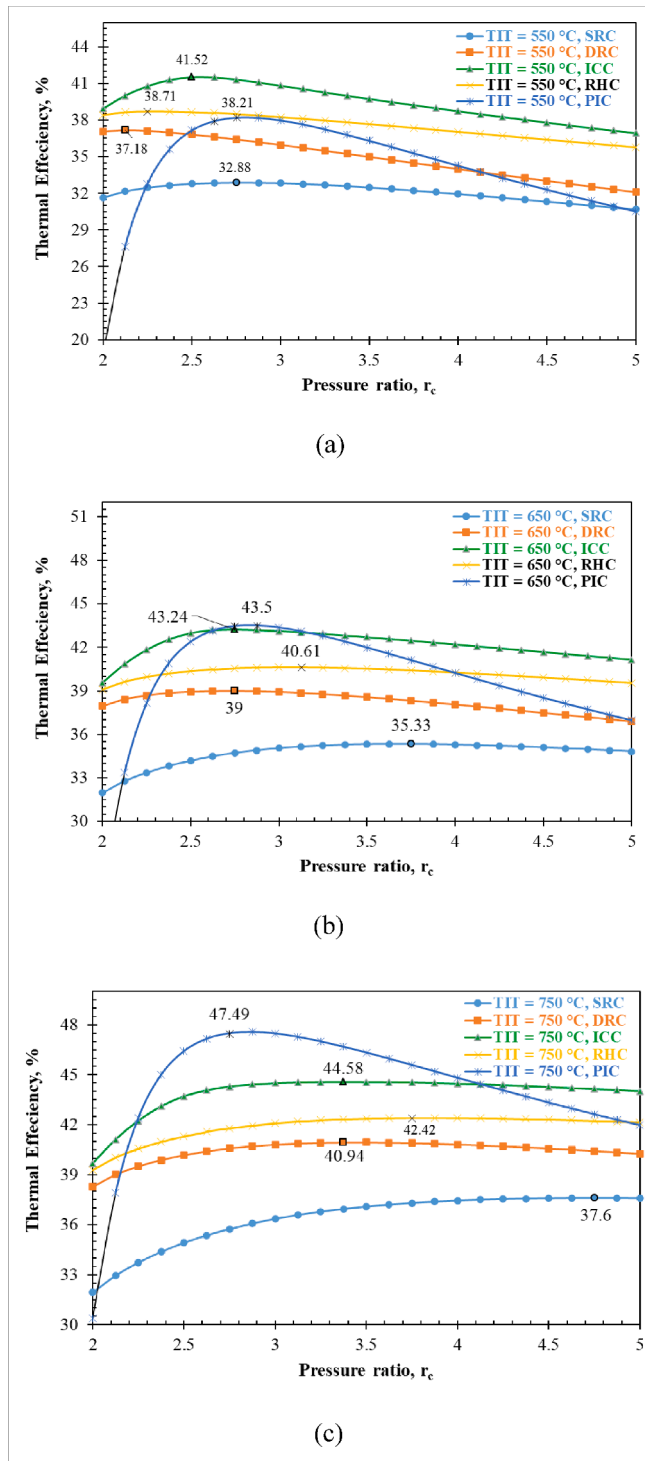


Fig. 12. Comparison of the layouts thermal efficiencies with the variation of the pressure ratio at TIT of a) 550 °C, b) 650 °C, and c) 750 °C. At fixed $P_{c,o} = 20$ MPa, $T_{c,i} = 50$ °C, $RPR = 0.3$.

turbine is higher than the increase of that consumed by the compressor up to the optimum value of the r_c . It is found that the optimum pressure is near to or less than the critical pressure of the CO_2 . This returns to that the gap between the pressure line increases significantly at temperatures higher than 40 °C and pressures lower than the critical pressure as shown in Fig. 11.

Also, it is found that higher r_c occurs at higher TIT with higher thermal efficiency. For instance, at TIT of 550 °C, the maximum

efficiency is 32.87% at an optimum r_c of 2.75. While at 750 °C, the maximum thermal efficiency is 37.6% at an optimum r_c of 4.88 as shown in Fig. 10 (a). Similar results are obtained for the other configurations except for the partial intercooling one, Fig. 10 (e), where optimum r_c values of the partial intercooling cycle seems to be the same ($r_c \approx 2.8$) regardless of the TIT.

It is obvious that higher TIT yields higher thermal efficiency since the specific volume increases with the temperature, which also increases the produced work through the expansion process. However, the effect of the TIT on the thermal efficiency is reduced at lower pressure ratios except for the partial intercooling cycle (PIC). The thermal efficiency at r_c of 2 is almost the same for the three selected TITs for each individual configuration (SRC, DRC, ICC and RHC) as shown in Fig. 10 (a, b, c, and d). Overall, the highest efficiency of 47.57% was achieved in PIC configuration at $r_c \approx 2.88$.

Fig. 12 compares the thermal efficiencies of all five configurations at TIT of 550 °C, Fig. 12 (a); 650 °C, Fig. 12 (b) and 750 °C, Fig. 12 (c). This comparison is carried out at $P_{c,o} = 20$ MPa, $T_{c,i} = 50$ °C and $RPR = 0.3$, where PRP is the intermediate pressure ratio defined by Eq. (32) in section 4.2. It is noted that the thermal efficiency of the ICC is higher than that of the other cycles except the PIC at TIT of 750 °C within the r_c range of 2.25 to 4.12. Table 7 presents a comparison between the studied layouts at the selected TITs. It is found that at $r_{c,min}$ of 2, the PIC has the lowest thermal efficiency while at $r_{c,max}$ of 5, the ICC has the maximum one. Furthermore, it is noticed that the higher TIT yields higher temperature at the inlet of the combustor $T_{co,i}$, which reduces the consumed fuel and improves the efficiency even if r_c remains constant as the case in the PIC as shown in the last two rows of Table 7. Within the design parameters shown in Table 4, the maximum efficiency of 47.57% is achieved by the PIC at an optimum r_c of 2.88 and TIT of 750 °C as mentioned above. At these conditions, the mass flow rate of the fuel is 1.89 kg/s. Also, the mass flow rates of the recycled sCO_2 , oxygen, produced sCO_2 , and water vapour are 445.70, 7.60, 450.90, and 4.22 kg/s, respectively.

For the results presented in Fig. 10 and Fig. 12 the effect of changing the compressor inlet pressure, the lower pressure $P_{c,i}$, was investigated by fixing the high-pressure at $P_{c,o} = 20$ MPa, while the pressure ratio was varied over its range (2–5). To study the effect of changing the high pressure, the compressor inlet pressure now is fixed at $P_{c,i} = 7.27$ MPa, while the pressure ratio is varied as shown in Fig. 13. It is noticed that the thermal efficiencies in Fig. 13 increase with the increase of r_c up to optimal values that are higher than obtained by changing the compressor inlet pressure (Fig. 12) except for the PIC. Over the range of r_c , the thermal efficiency of the PIC decreases since the increase of compression power is more than the improvement in the heat recovered from the LTR (see Fig. 13(c)). Furthermore, higher efficiencies are obtained at higher turbine inlet pressure (high r_c) compared to those obtained at $P_{c,o} = 20$ MPa for all configurations. However, at r_c higher than 4, the required turbine inlet pressure exceeds 30 MPa, which is over the maximum allowable pressure for the developed turbines [3].

4.2. Effect of the intermediate pressure ratio

The intermediate pressure is applicable only for the ICC, RHC, and PIC cycles that include two-stage compression or expansion process. In the ICC, the main compressor raises the pressure from the lower value ($P_{low} = P_{c,i}$) to the intermediate pressure (P_{im}), then the other compressor increases it to the high design pressure ($P_{high} = P_{c,o}$) after the intercooling process. Similarly, in the RHC, the combustion products expand in the first turbine to the P_{im} , then expand to the lower pressure across the second turbine after the reheating process. To explain the effect of the P_{im} on the thermal efficiency of the cycle, the intermediate pressure ratio (RPR) is defined as:

$$RPR = \frac{P_{c,o} - 1}{r_c - 1} \quad (32)$$

Table 7

Optimum pressure ratio and optimum efficiency of the studied layouts at different TITs at $P_{c,o} = 20$ MPa and $T_{c,i} = 50$ °C. $r_{c,min} = 2$, $r_{c,max} = 5$.

Layout	$P_{c,i}$ @ opt. MPa	$T_{c,o}$, °C	$r_{c,opt}$	$T_{co,i}$, °C	\dot{m}_{CH_4} , kg/s	$T_{t,i}$, °C	η_{th} @ $r_{c,min}$, %	η_{th} @ $r_{c,max}$, %	η_{opt} , %
SRC	7.27	135.80	2.75	395.80	2.74	550	31.64	30.69	32.88
	5.33	169.70	3.75	448.10	2.55	650	31.98	34.82	35.33
	4.87	196.50	4.87	500.60	2.39	750	31.93	37.59	37.60
DRC	9.41	101.70	2.13	434.00	2.42	550	37.06	32.09	37.20
	7.27	135.80	2.75	493.70	2.31	650	37.96	36.91	39.00
	5.93	158.50	3.38	555.00	2.20	750	38.28	40.27	40.94
ICC	8.00	83.98	2.50	415.50	2.17	550	38.94	36.84	41.51
	7.27	96.02	2.75	489.80	2.09	650	39.55	41.00	43.19
	5.93	120.30	3.38	551.2	2.03	750	39.65	43.83	44.47
RHC	8.89	110.20	2.25	479.60	2.15	550	38.41	35.75	38.71
	6.67	145.70	3.00	563.40	2.05	650	39.09	39.54	40.61
	5.33	169.70	3.75	647.90	1.97	750	39.28	42.15	42.42
PIC	7.27	118.80	2.75	416.00	2.36	550	19.01	30.53	38.21
	6.96	121.80	2.88	501.60	2.07	650	25.30	37.30	43.50
	6.96	121.80	2.88	592.20	1.89	750	30.37	42.00	47.57

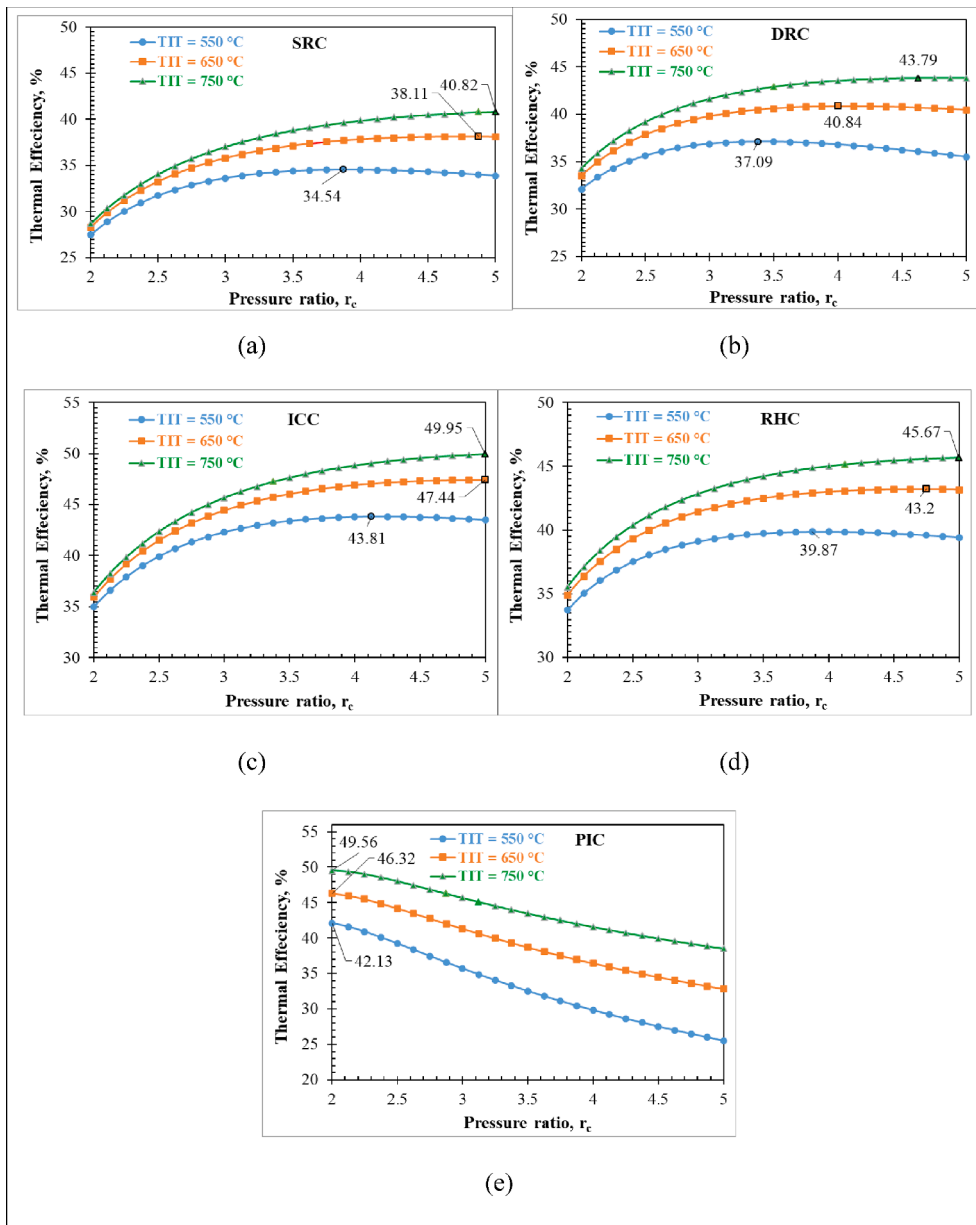


Fig. 13. Effect of the pressure ratio (r_c) on the thermal efficiency of the studied layouts at different inlet turbine temperatures. At fixed $P_{c,i} = 7.27$ MPa, $T_{c,i} = 50$ °C, RPR = 0.60.

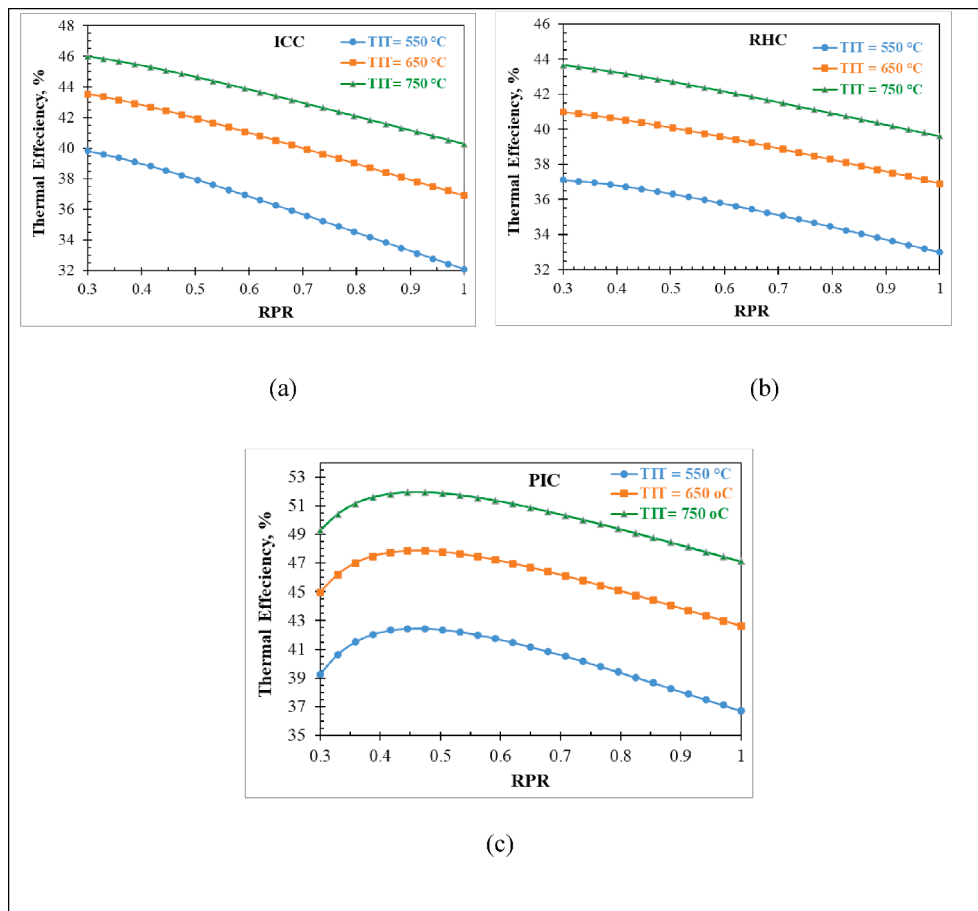


Fig. 14. Effect of the intermediate pressure ratio on the thermal efficiency of a) ICC, b) RHC, and c) PIC at different TITs.

Table 8

Optimum RPR and optimum efficiency of the studied layouts at different TITs at $P_{c,o} = 20$ MPa, $T_{c,i} = 50$ °C, $r_c = 5$.

Layout	$P_{im,opt}$, MPa	$T_{c,o}$, °C	RPR_{opt}	$T_{c,i}$, °C	\dot{m}_{CH_4} , kg/s	$T_{t,i}$, °C	$\eta_{th}@ RPR_{min}$, %	$\eta_{th}@ RPR_{max}$, %	η_{opt} , %
ICC	9.09	106.90	0.30	351.20	2.26	550	39.82	32.09	39.82
	9.09	106.90	0.30	429.20	2.07	650	43.53	36.91	43.53
	9.09	106.90	0.30	506.90	1.96	750	45.99	40.27	45.99
RHC	9.25	199.10	0.30	427.50	2.24	550	37.11	32.98	37.11
	9.25	199.10	0.30	510.30	2.03	650	40.98	36.90	40.98
	9.25	199.10	0.30	593.00	1.90	750	43.65	39.61	43.65
PIC	6.90	138.50	0.48	349.10	2.12	550	39.27	36.72	42.45
	6.90	138.50	0.48	434.30	1.88	650	44.95	42.62	47.86
	7.18	134.6	0.48	520.20	1.74	750	49.27	47.14	51.93

Based on Eq. (32), higher RPR means lower intermediate pressure (P_{im}) with fixed pressure ratio (r_c). Fig. 14 shows the relationship between the thermal efficiency and the RPR at different TITs. As shown in Fig. 14 (a and b), the increase of the RPR reduces the thermal efficiency of the ICC and RHC cycles because P_{im} decreases with the increase of the RPR, which limits the compression and/or the expansion process in the first stage. Fig. 14 (c) shows that there is an optimum RPR of 0.48 for the PIC cycle and is not affected by the variation of the TIT. Furthermore, the thermal efficiency always improves by increasing TIT due to the increase of the temperature at the inlet of the combustor ($T_{c,i}$) with no effect on the trend of the relation between the thermal efficiency and the RPR.

Table 8 shows the major performance parameters of the studied layouts at the optimum RPR and the selected TITs. It is found that the maximum thermal efficiency of 51.93% is achieved by the PIC at RPR_{opt} of 0.48 and TIT of 750 °C and the lowest thermal efficiency of 37.11% is obtained by the RHC at RPR_{opt} of 0.3 and TIT of 550 °C. Fig. 15 compares

the thermal efficiency of the ICC, RHC, and PIC with the increase of the RPR at different TITs at r_c of 5, $P_{c,o} = 20$ MPa, and $T_{c,i} = 50$ °C. At these conditions, the thermal efficiency of the PIC is superior compared to that of the ICC and RHC. Furthermore, the thermal efficiency of the ICC is higher than that of the RHC except at TIT of 550 °C and RPR higher than 0.85 as shown in Fig. 15 (a).

4.3. Effect of the turbine inlet temperature

Fig. 16 shows the effect of the turbine inlet temperature (TIT) of the studied layouts at r_c of 4, RPR of 0.6, and $T_{c,i} = 50$ °C. At these conditions, the highest thermal efficiency is achieved by the PIC and the lowest is achieved by the SRC. Comparing the thermal efficiency of the studied layouts relative to that of the SRC, it can be noted that the thermal efficiencies of the DRC, ICC, RHC, and PIC cycles are higher than of the SRC by about 2%, 6%, 5%, and 12%, respectively. The PIC archives the highest efficiency due to the higher inlet temperature at the

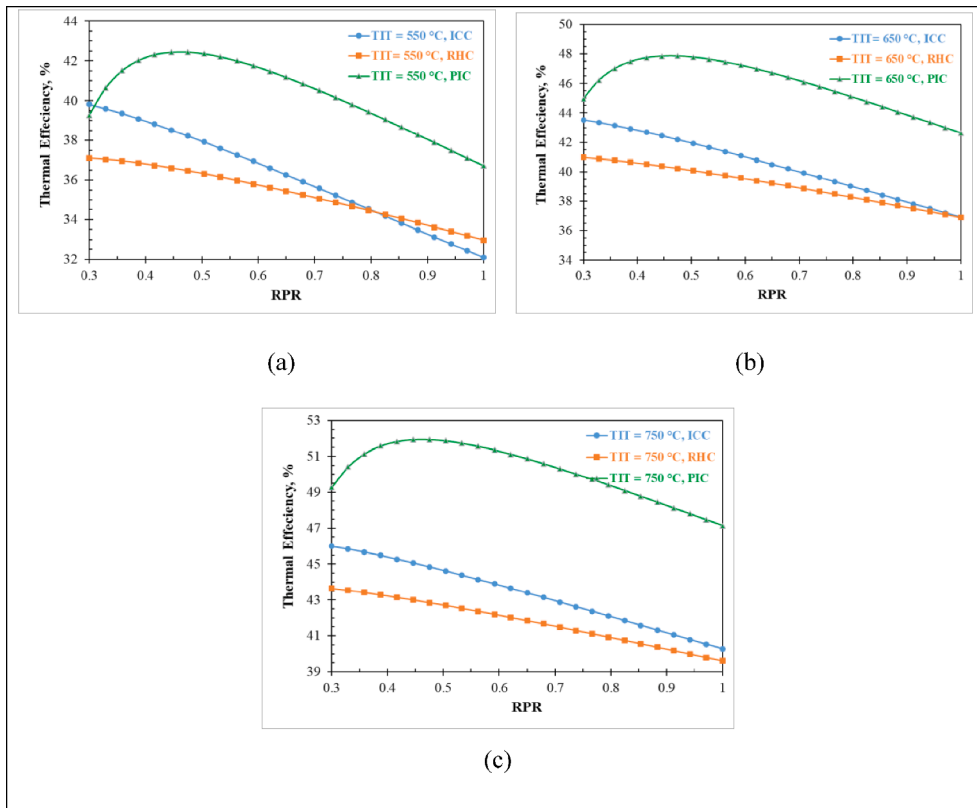


Fig. 15. Comparison of the thermal efficiency of ICC, RHC, and PIC with the variation of the RPR at TIT of a) 550 °C, b) 650 °C, and c) 750 °C. At $r_c = 5$.

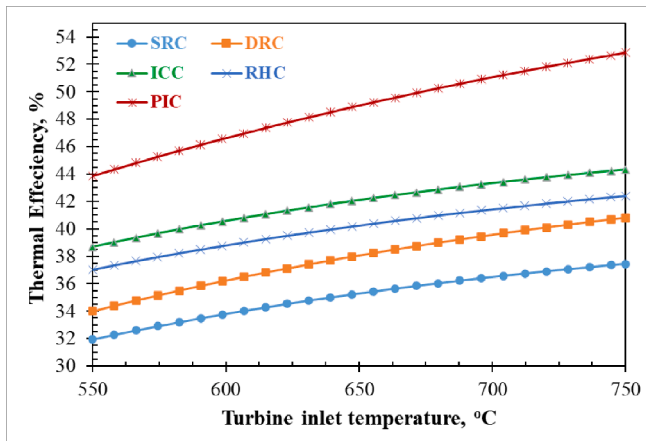


Fig. 16. Effect of the TIT on the thermal efficiency of the studied layouts. At $P_{c,o} = 20$ MPa, $r_c = 4$, $T_{c,i} = 50$ C and RPR = 0.6.

inlet of the combustor, which reduces the amount of the consumed fuel to reach the desired TIT.

4.4. Effect of the compressor inlet temperature

One of the major parameters that affect the performance of the compressor as well as the overall thermal efficiency of the system is the temperature at the inlet of the compressor (CIT). Fig. 17 compares the thermal efficiency of the studied cycles with the variation of the CIT at TIT = 750 °C, $P_{c,o} = 20$ MPa, $r_c = 4$, and RPR = 0.6. The temperature at the inlet of the compressor depends on whether the precooling process is performed by water (wet) or by dry air. For wet cooling conditions, the CIT is set at 35 °C while for dry air conditions, the CIT is set at 50 °C.

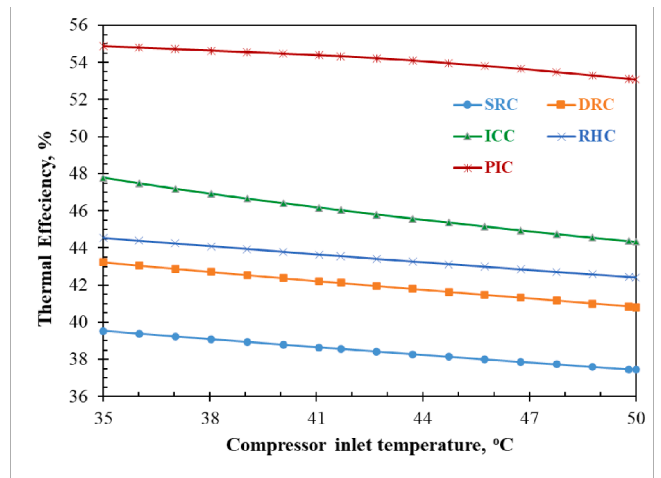


Fig. 17. Effect of the CIT on the thermal efficiency of the studied layout temperature.

Through this range, the thermal efficiency of the studied layouts decreases almost linearly with the increase of the CIT. This is attributed to the increase of the specific volume of the sCO_2 with the temperature, which requires more power to perform the compression process. The increase of the CIT from 35 °C to 50 °C reduced the thermal efficiency of the studied cycles by about 2%.

Fig. 18 shows the effect of the CIT on the optimum value of the RPR at different r_c for the ICC layout to obtain the maximum thermal efficiency and exergy efficiency (which is discussed for all configurations in section 4.5). It is noted that the increase of the CIT reduces the value of the optimum RPR, which means higher intermediate pressure is required for better performance. Also, the optimum RPR is affected by

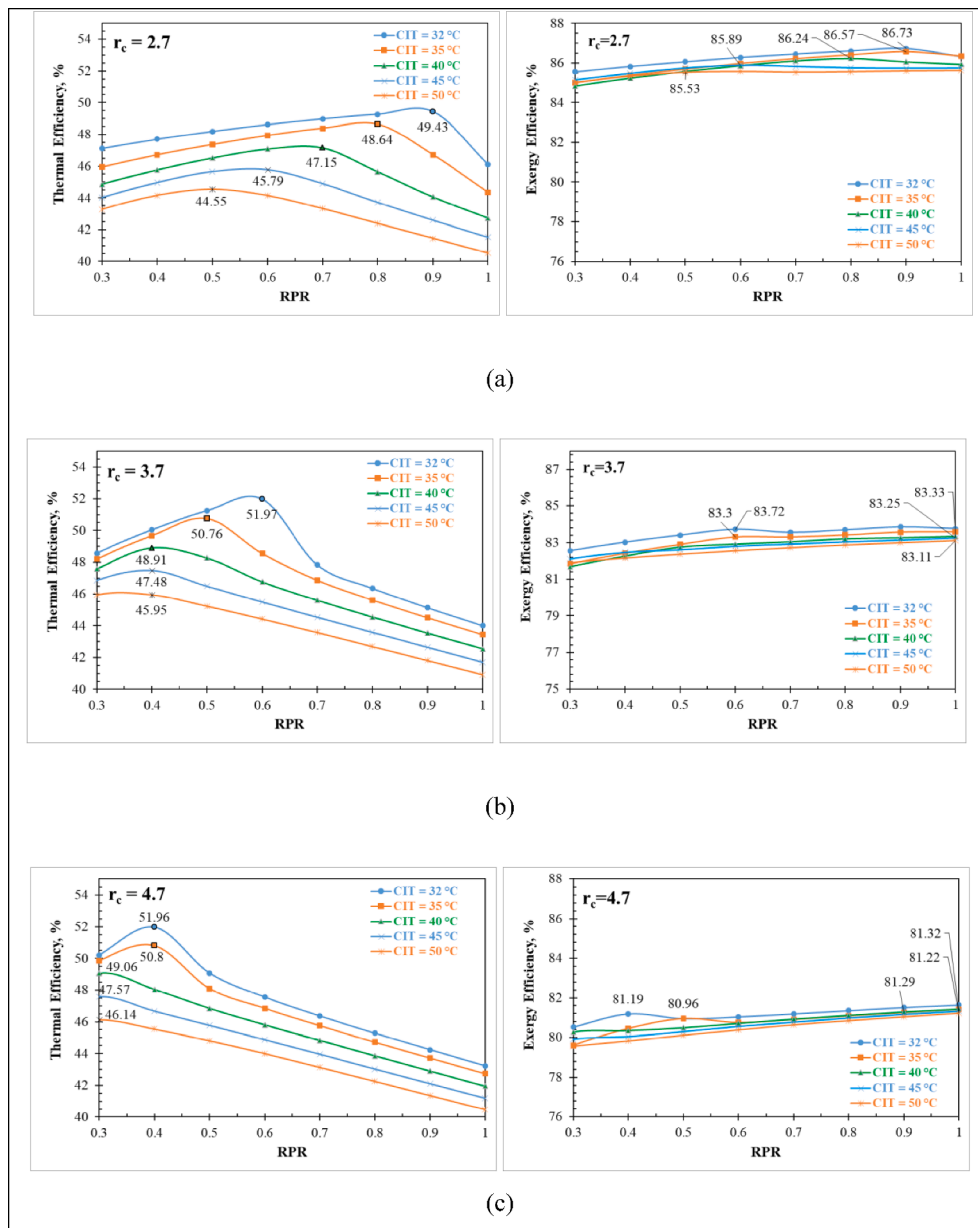


Fig. 18. Effect of the RPR ratio on the thermal efficiency and the exergy efficiency of the ICC at different CITs at pressure ratio of (a) $r_c = 2.7$, b) $r_c = 3.7$, and c) $r_c = 4.7$. At TIT = 750 °C, $P_{c,o} = 20$ MPa.

the value of the r_c since it decreases at higher r_c . For instance, at CIT = 32 °C and $r_c = 2.7$, the $RPR_{opt} = 0.9$, while at $r_c = 4.7$ with the same CIT, the $RPR_{opt} = 0.4$. (see Fig. 18 (a, c)). The exergy efficiency increases up to an optimum RPR value then slightly decreases for higher RPR values (see Fig. 18 (a,b, and c)). At CIT of 32 °C (which is close to the critical temperature of the CO₂ (30.9 °C)), the optimum RPR for the maximum thermal efficiency is identical to that for the maximum exergy efficiency. However, as the CIT increases, the optimum RPR for maximum efficiency deviates from that for the maximum exergy efficiency. Furthermore, the increase of the CIT positively affects the exergy efficiency of the recuperator and negatively affects the exergy efficiency of the pre-cooler, compressor, and the combustor. Therefore, the overall exergy efficiency of the ICC decreases with the increase of the CIT. However, the increase of the pressure ratio reduces the exergy efficiency more than the decrease associated with the increase of CIT. For instance, at $r_c = 2.7$ and $RPR = 0.9$, the increases of the CIT from 32 °C to 50 °C reduces the exergy efficiency by 1.13%, while the increase of the pressure ratio from 2.7 to 3.7 (at $RPR = 0.9$ and CIT = 32 °C) reduces the exergy

Table 9

Comparison of the second law efficiency of the cycle components at TIT = 750 °C, CIT = 35 °C, $r_c = 4$, RPR = 0.6;

Component	Second law efficiency (%)				
	SRC	DRC	ICC	RHC	PIC
Combustor(s)	67.24	71.26	70.51	90.15	71.53
Turbine(s)	95.90	95.93	95.92	78.46	97.86
Recuperator(s)	85.13	89.67	92.56	90.35	76.8
Compressor(s)	96.64	96.64	96.12	96.64	90.04
Intercooler	-	-	87.69	-	96.55
Precooler	73.22	76.27	80.77	73.34	81.35
Overall system	79.68	82.52	81.87	88.07	80.63

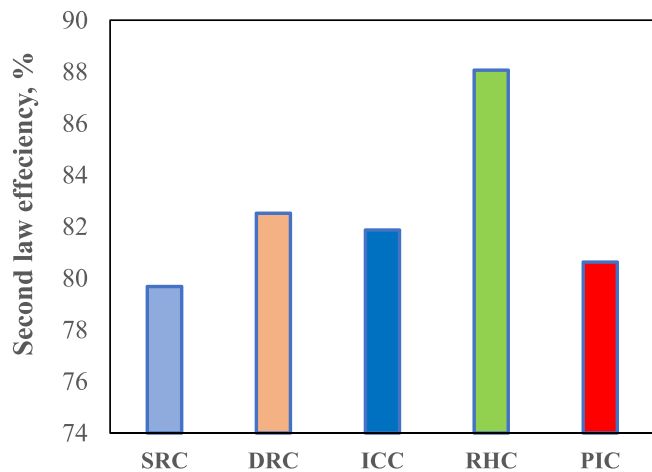


Fig. 19. Overall second law efficiency of the studied layouts at $T_{t,i} = 750\text{ }^{\circ}\text{C}$, $T_{c,i} = 50\text{ }^{\circ}\text{C}$, $r_c = 4$, $\text{RPR} = 0.6$;

efficiency by 2.88%.

4.5. Exergy performance of the system

In this section, the exergy efficiencies of each component (or process) of the studied configurations at $\text{TIT} = 750\text{ }^{\circ}\text{C}$, $\text{CIT} = 50\text{ }^{\circ}\text{C}$, $r_c = 4$, $\text{RPR} = 0.6$ are presented in Table 9. It can be noted that the lowest exergy efficiency (second law efficiency) is for the combustor except in the RHC layout. This is mainly explained by the chemical reactions that increase its irreversibility rate. Also, the exergy performance of the precooler is considerably poor due to the large temperature difference between the hot combustion products and the cooling fluid (water). The exergy performance of the turbines and compressors is superior relative to the other components. This is partially explained by the assumption of no heat transfer through their walls to the environment. As shown in Fig. 19, the overall second law efficiency of the SRC is the minimum ($\eta_{II,SRC} = 79.16\%$), while the maximum is for the RHC ($\eta_{II,RHC} = 88.07\%$).

5. Conclusions

Important research gaps related to supercritical carbon dioxide (sCO_2) power cycles are investigated in this study including the effects of adding extra components, operation at moderate temperature levels and using direct oxy-combustion (DOC) for sCO_2 power cycles. Energy and exergy analyses of five novel sCO_2 power cycle configurations driven by DOC are introduced. The studied cycle configurations were carefully selected based on their potential performance, suitability of integration with DOC, and controllability of their limitations. The configurations are: the simple recuperator cycle (SRC), dual recuperator cycle (DRC), intercooling cycle (ICC), reheating cycle (RHC) and partial intercooling cycle (PIC). The analyses investigate the effects of the major operating parameters on the thermal and second law efficiencies. To account for the variations in CO_2 properties with temperature, a discretised multi-segment numerical model was developed for the detail calculations of the recuperators. The effects of the low and high pressures of the cycles at inlet turbine temperature of $550\text{ }^{\circ}\text{C}$, $650\text{ }^{\circ}\text{C}$ and $750\text{ }^{\circ}\text{C}$ for a net output power of 50 MW are investigated. Based on the results, the following is concluded:

At the cycle level:

- There is an optimal pressure ratio (r_c) and intermediate pressure ratio (RPR) for which the highest efficiency is obtained. PIC configuration achieved the highest efficiencies of 47.57% and 51.93% at $r_{c,opt}$ of 2.88 and RPR_{opt} of 0.48, respectively.

- The maximum thermal efficiency of 52% is achieved by the PIC at r_c of 5, RPR of 0.45, TIT of $750\text{ }^{\circ}\text{C}$, high pressure of 20 MPa, and CIT of $50\text{ }^{\circ}\text{C}$.
- The reheating cycle has the highest second law efficiency with marginal improvement in the thermal efficiency compared to the dual recuperator cycle (DRC).
- The SRC has the simplest structure, however with the lowest thermal and second law efficiencies.
- The PIC has superior performance compared to the other configurations at higher TIT and lower RPR.
- The RHC is more complex than DRC with only marginal improvement in the thermal efficiency.
- The highest second law efficiency is achieved by the RHC, while the lowest one is for the SRC.

At the component level:

- The temperature at the inlet of the compressor (CIT) has considerable effect on the intermediate pressure ratio.
- The combustor has the lowest second law efficiency except for the RHC.

CRediT authorship contribution statement

Ahmad K. Sleiti: Conceptualization, Investigation, Writing - original draft, Writing - review & editing, Funding acquisition, Supervision.
Wahib A. Al-Ammari: Conceptualization, Writing - original draft, Writing - review & editing, Visualization.

Declaration of Competing Interest

The authors declare that they have no known competing financial interests or personal relationships that could have appeared to influence the work reported in this paper.

Acknowledgement

The work presented in this publication was made possible by NPRP-S grant # [11S-1231-170155] from the Qatar National Research Fund (a member of Qatar Foundation). The findings herein reflect the work, and are solely the responsibility, of the authors. Open Access funding provided by the Qatar National Library.

References

- [1] Crespi F, Gavagnin G, Sánchez D, Martínez GS. Supercritical carbon dioxide cycles for power generation: A review. *Appl Energy* 2017;195:152–83. <https://doi.org/10.1016/j.apenergy.2017.02.048>.
- [2] Li MJ, Zhu HH, Guo JQ, Wang K, Tao WQ. The development technology and applications of supercritical CO_2 power cycle in nuclear energy, solar energy and other energy industries. *Appl Therm Eng* 2017;126:255–75. <https://doi.org/10.1016/j.applthermaleng.2017.07.173>.
- [3] White MT, Bianchi G, Chai L, Tassou SA, Sayma AI. Review of supercritical CO_2 technologies and systems for power generation. *Appl Therm Eng* 2021;185:116447. <https://doi.org/10.1016/j.applthermaleng.2020.116447>.
- [4] Wang X, Li X, Li Q, Liu L, Liu C. Performance of a solar thermal power plant with direct air-cooled supercritical carbon dioxide Brayton cycle under off-design conditions. *Appl Energy* 2020;261:114359. <https://doi.org/10.1016/j.apenergy.2019.114359>.
- [5] Kouta A, Al-Sulaiman FA, Atif M. Energy analysis of a solar driven cogeneration system using supercritical CO_2 power cycle and MEE-TVC desalination system. *Energy* 2017;119:996–1009. <https://doi.org/10.1016/j.energy.2016.11.041>.
- [6] Stein WH, Buck R. Advanced power cycles for concentrated solar power. *Sol Energy* 2017;152:91–105. <https://doi.org/10.1016/j.solener.2017.04.054>.
- [7] Linares JI, Montes MJ, Cantizano A, Sánchez C. A novel supercritical CO_2 recompression Brayton power cycle for power tower concentrating solar plants. *Appl Energy* 2020;263:114644. <https://doi.org/10.1016/j.apenergy.2020.114644>.
- [8] Manente G, Fortuna FM. Supercritical CO_2 power cycles for waste heat recovery: A systematic comparison between traditional and novel layouts with dual expansion. *Energy Convers Manag* 2019;197:111777. <https://doi.org/10.1016/j.enconman.2019.111777>.

- [9] Liang Y, Bian X, Qian W, Pan M, Ban Z, Yu Z. Theoretical analysis of a regenerative supercritical carbon dioxide Brayton cycle/organic Rankine cycle dual loop for waste heat recovery of a diesel/natural gas dual-fuel engine. *Energy Convers Manag* 2019;197:111845. <https://doi.org/10.1016/j.enconman.2019.111845>.
- [10] Feng Y, Du Z, Shreka M, Zhu Y, Zhou S, Zhang W. Thermodynamic analysis and performance optimization of the supercritical carbon dioxide Brayton cycle combined with the Kalina cycle for waste heat recovery from a marine low-speed diesel engine. *Energy Convers Manag* 2020;206:112483. <https://doi.org/10.1016/j.enconman.2020.112483>.
- [11] Wu C, Wang S, Li J. Exergoeconomic analysis and optimization of a combined supercritical carbon dioxide recompression Brayton/organic flash cycle for nuclear power plants. *Energy Convers Manag* 2018;171:936–52. <https://doi.org/10.1016/j.enconman.2018.06.041>.
- [12] Moiseyev A, Sienicki JJ. Investigation of alternative layouts for the supercritical carbon dioxide Brayton cycle for a sodium-cooled fast reactor. *Nucl Eng Des* 2009; 239:1362–71. <https://doi.org/10.1016/j.nucengdes.2009.03.017>.
- [13] Qiao Z, Cao Y, Li P, Wang X, Romero CE, Pan L. Thermo-economic analysis of a CO₂ plume geothermal and supercritical CO₂ Brayton combined cycle using solar energy as auxiliary heat source. *J Clean Prod* 2020;256:120374. <https://doi.org/10.1016/j.jclepro.2020.120374>.
- [14] Ruiz-Casanova E, Rubio-Maya C, Pacheco-Ibarra JJ, Ambriz-Díaz VM, Romero CE, Wang X. Thermodynamic analysis and optimization of supercritical carbon dioxide Brayton cycles for use with low-grade geothermal heat sources. *Energy Convers Manag* 2020;216:112978. <https://doi.org/10.1016/j.enconman.2020.112978>.
- [15] Bae SJ, Ahn Y, Lee J, Lee JI. Various supercritical carbon dioxide cycle layouts study for molten carbonate fuel cell application. *J Power Sources* 2014;270: 608–18. <https://doi.org/10.1016/j.jpowsour.2014.07.121>.
- [16] Chen Y, Wang M, Liso V, Samsatli S, Samsatli NJ, Jing R, et al. Parametric analysis and optimization for exergoeconomic performance of a combined system based on solid oxide fuel cell-gas turbine and supercritical carbon dioxide Brayton cycle. *Energy Convers Manag* 2019;186:66–81. <https://doi.org/10.1016/j.enconman.2019.02.036>.
- [17] Schöffner SI, Klein SA, Aravind PV, Pecnik R. A solid oxide fuel cell- supercritical carbon dioxide Brayton cycle hybrid system. *Appl Energy* 2020. <https://doi.org/10.1016/j.apenergy.2020.115748>.
- [18] Weiland NT, White CW. Techno-economic analysis of an integrated gasification direct-fired supercritical CO₂ power cycle. *Fuel* 2018;212:613–25. <https://doi.org/10.1016/j.fuel.2017.10.022>.
- [19] Liu Y, Wang Y, Huang D. Supercritical CO₂ Brayton cycle: A state-of-the-art review. *Energy* 2019;189:115900. <https://doi.org/10.1016/j.energy.2019.115900>.
- [20] Olumayegun O, Wang M. Dynamic modelling and control of supercritical CO₂ power cycle using waste heat from industrial processes. *Fuel* 2019;249:89–102. <https://doi.org/10.1016/j.fuel.2019.03.078>.
- [21] Zhao D, Zhao R, Deng S, Zhao L, Chen M. Transcritical carbon dioxide power cycle for waste heat recovery: A roadmap analysis from ideal cycle to real cycle with case implementation. *Energy Convers Manag* 2020;226:113578. <https://doi.org/10.1016/j.enconman.2020.113578>.
- [22] Kim YM, Kim CG, Favrat D. Transcritical or supercritical CO₂ cycles using both low- and high-temperature heat sources. *Energy* 2012;43:402–15. <https://doi.org/10.1016/j.energy.2012.03.076>.
- [23] Guo J. Design analysis of supercritical carbon dioxide recuperator. *Appl Energy* 2016;164:21–7. <https://doi.org/10.1016/j.apenergy.2015.11.049>.
- [24] Scaccabarozzi R, Gatti M, Martelli E. Thermodynamic analysis and numerical optimization of the NET Power oxy-combustion cycle. *Appl Energy* 2016;178: 505–26. <https://doi.org/10.1016/j.apenergy.2016.06.060>.
- [25] Ahn Y, Bae SJ, Kim M, Cho SK, Baik S, Lee JI, et al. Review of supercritical CO₂ power cycle technology and current status of research and development. *Nucl Eng Technol* 2015;47:647–61. <https://doi.org/10.1016/j.net.2015.06.009>.
- [26] Purjam M, Goudarzi K, Keshtgar M. A New Supercritical Carbon Dioxide Brayton Cycle with High Efficiency. *Heat Transf Asian Res* 2017;46:465–82. <https://doi.org/10.1002/hjt.21225>.
- [27] Padilla RV, Too YCS, Benito R, McNaughton R, Stein W. Thermodynamic feasibility of alternative supercritical CO₂ Brayton cycles integrated with an ejector. *Appl Energy* 2016;169:49–62. <https://doi.org/10.1016/j.apenergy.2016.02.029>.
- [28] Turchi CS, Ma Z, Neises TW, Wagner MJ. Thermodynamic study of advanced supercritical carbon dioxide power cycles for concentrating solar power systems. *J Sol Energy Eng Trans ASME* 2013;135:1–7. <https://doi.org/10.1115/1.4024030>.
- [29] Shublaq M, Sleiti AK. Experimental analysis of water evaporation losses in cooling towers using filters. *Appl Therm Eng* 2020;175:115418.
- [30] Sleiti AK, Al-Ammari WA, Al-Khawaja M. Review of innovative approaches of thermo-mechanical refrigeration systems using low grade heat. *Int J Energy Res* 2020;44. <https://doi.org/10.1002/er.5556>.
- [31] Allam R, Martin S, Forrest B, Fetvedt J, Lu X, Freed D, et al. Demonstration of the Allam Cycle: An Update on the Development Status of a High Efficiency Supercritical Carbon Dioxide Power Process Employing Full Carbon Capture. *Energy Procedia* 2017;114:5948–66. <https://doi.org/10.1016/j.egypro.2017.03.1731>.
- [32] Mathieu P, Nihart R. Zero-emission MATIANT cycle. *J Eng Gas Turbines Power* 1999;121:116–20. <https://doi.org/10.1115/1.2816297>.
- [33] Zhao Y, Chi J, Zhang S, Xiao Y. Thermodynamic study of an improved MATIANT cycle with stream split and recompression. *Appl Therm Eng* 2017;125:452–69. <https://doi.org/10.1016/j.applthermaleng.2017.05.023>.
- [34] Yantovski EI, Zvagolsky KN, Gavrilenko VA. The COOPERATE-demo power cycle. *Energy Convers Manag* 1995;36:861–4. [https://doi.org/10.1016/0196-8904\(95\)00139-5](https://doi.org/10.1016/0196-8904(95)00139-5).
- [35] McClung A, Brun K, Chordia L. Technical and economic evaluation of supercritical oxy-combustion for power generation. *Fourth Supercrit. CO₂ Power Cycles Symp.* Pittsburgh, PA, Sept, Pittsburgh, Pennsylvania: 2014, p. 1–14.
- [36] Zhang N, Lior N. A novel near-zero CO₂ emission thermal cycle with LNG cryogenic exergy utilization. *Energy* 2006;31:1666–79. <https://doi.org/10.1016/j.energy.2005.05.006>.
- [37] Gatewood J, Moore J, Ph D, Brun K, Ph D. The Texas Cryogenic Oxy-Fuel Cycle (TCO): A Novel Approach to Power Generation With CO₂ Options 2013:1007–14. 10.1115/GT2012-69930.
- [38] Allam RJ, Fetvedt JE, Forrest BA, Freed DA. The OXY-fuel, supercritical CO₂ allam cycle: New cycle developments to produce even lower-cost electricity from fossil fuels without atmospheric emissions. *Proc ASME Turbo Expo* 2014;GT2014-269: 1–9. 10.1115/GT2014-26952.
- [39] Ekici S. Thermodynamic mapping of A321–200 in terms of performance parameters, sustainability indicators and thermo-ecological performance at various flight phases. *Energy* 2020;202:117692. <https://doi.org/10.1016/j.energy.2020.117692>.
- [40] Dinc A, Şöhret Y, Ekici S. Exergy analysis of a three-spool turbo-prop engine during the flight of a cargo aircraft. *Aircr Eng Aerosp Technol* 2020;92:1495–503. <https://doi.org/10.1108/AEAT-05-2020-0087>.
- [41] Ekici S. Investigating routes performance of flight profile generated based on the off-design point: Elaboration of commercial aircraft-engine pairing. *Energy* 2020; 193:116804. <https://doi.org/10.1016/j.energy.2019.116804>.
- [42] Şöhret Y, Ekici S, Altuntaş Ö, Hepbasli A, Karakoç TH. Exergy as a useful tool for the performance assessment of aircraft gas turbine engines: A key review. *Prog Aerosp Sci* 2016;83:57–69. <https://doi.org/10.1016/j.paerosci.2016.03.001>.
- [43] Zhou J, Ling P, Su S, Xu J, Xu K, Wang Y, et al. Exergy analysis of a 1000 MW single reheat advanced supercritical carbon dioxide coal-fired partial flow power plant. *Fuel* 2019;255:115777. <https://doi.org/10.1016/j.fuel.2019.115777>.
- [44] Luo J, Emelogu O, Morosuk T, Tsatsaronis G. Exergy-based investigation of a coal-fired allam cycle. *Energy* 2021;218:119471. <https://doi.org/10.1016/j.energy.2020.119471>.
- [45] Chen Z, Wang Y, Zhang X. Energy and exergy analyses of S-CO₂ coal-fired power plant with reheating processes. *Energy* 2020;211:118651. <https://doi.org/10.1016/j.energy.2020.118651>.
- [46] Javani N, Dincer I, Naterer GF. Thermodynamic analysis of waste heat recovery for cooling systems in hybrid and electric vehicles. *Energy* 2012;46:109–16. <https://doi.org/10.1016/j.energy.2012.02.027>.
- [47] Hamut HS, Dincer I, Naterer GF. Exergy analysis of a TMS (thermal management system) for range-extended EVs (electric vehicles). *Energy* 2012;46:117–25. <https://doi.org/10.1016/j.energy.2011.12.041>.
- [48] Yu A, Su W, Lin X, Zhou N, Zhao L. Thermodynamic analysis on the combination of supercritical carbon dioxide power cycle and transcritical carbon dioxide refrigeration cycle for the waste heat recovery of shipboard. *Energy Convers Manag* 2020;221:113214. <https://doi.org/10.1016/j.enconman.2020.113214>.
- [49] Li B, Wang S, Wang K, Song L. Comparative investigation on the supercritical carbon dioxide power cycle for waste heat recovery of gas turbine. *Energy Convers Manag* 2021;228. <https://doi.org/10.1016/j.enconman.2020.113670>.
- [50] Abid M, Khan MS, Ratlamwala TAH. Comparative energy, exergy and exergoeconomic analysis of solar driven supercritical carbon dioxide power and hydrogen generation cycle. *Int J Hydrogen Energy* 2020;45:5653–67. <https://doi.org/10.1016/j.ijhydene.2019.06.103>.
- [51] Atif M, Al-Sulaiman FA. Energy and exergy analyses of solar tower power plant driven supercritical carbon dioxide recompression cycles for six different locations. *Renew Sustain Energy Rev* 2017;68:153–67. <https://doi.org/10.1016/j.rser.2016.09.122>.
- [52] Yang H, Li J, Wang Q, Wu L, Reyes Rodríguez-Sánchez M, Santana D, et al. Performance investigation of solar tower system using cascade supercritical carbon dioxide Brayton-steam Rankine cycle. *Energy Convers Manag* 2020;225:113430. <https://doi.org/10.1016/j.enconman.2020.113430>.
- [53] AlZahrani AA, Dincer I. Energy and exergy analyses of a parabolic trough solar power plant using carbon dioxide power cycle. *Energy Convers Manag* 2018;158: 476–88. <https://doi.org/10.1016/j.enconman.2017.12.071>.
- [54] Khatoun S, Kim MH. Performance analysis of carbon dioxide based combined power cycle for concentrating solar power. *Energy Convers Manag* 2020;205: 112416. <https://doi.org/10.1016/j.enconman.2019.112416>.
- [55] Ganjehsarabi H, Gungor A, Dincer I. Exergetic performance analysis of Dora II geothermal power plant in Turkey. *Energy* 2012;46:101–8. <https://doi.org/10.1016/j.energy.2012.02.039>.
- [56] Ji-chao Y, Sobhani B. Integration of Biomass Gasification with a Supercritical CO₂ and Kalina Cycles in a Combined Heating and Power System: A Thermodynamic and Exergoeconomic Analysis. *Energy* 2021;222:119980. <https://doi.org/10.1016/j.energy.2021.119980>.
- [57] Mousapour A, Hajipour A, Rashidi MM, Freidoonimehr N. Performance evaluation of an irreversible Miller cycle comparing FTT (finite-time thermodynamics) analysis and ANN (artificial neural network) prediction. *Energy* 2016;94:100–9. <https://doi.org/10.1016/j.energy.2015.10.073>.
- [58] Valencia Ochoa G, Duarte Forero J, Rojas JP. A comparative energy and exergy optimization of a supercritical-CO₂ Brayton cycle and Organic Rankine Cycle combined system using swarm intelligence algorithms. *Heliyon* 2020;6:e04136. <https://doi.org/10.1016/j.heliyon.2020.e04136>.
- [59] Talebizadehsardari P, Ehyaei MA, Ahmadi A, Jamali DH, Shirmohammadi R, Eyyvazian A, et al. Energy, exergy, economic, exergoeconomic, and exergoenvironmental (5E) analyses of a triple cycle with carbon capture. *J CO₂ Util* 2020;41:101258. 10.1016/j.jcou.2020.101258.

- [60] Schöffner SI, Klein SA, Aravind PV, Pecnik R. A solid oxide fuel cell- supercritical carbon dioxide Brayton cycle hybrid system. *Appl Energy* 2021;283:115748. <https://doi.org/10.1016/j.apenergy.2020.115748>.
- [61] Rashidi MM, Parsa AB, Shamekhi L, Nazari F, Ali M. Exergetic optimisation of a multi-stage compression transcritical refrigeration cycle. *Int J Exergy* 2016;20:22–47. <https://doi.org/10.1504/IJEX.2016.076677>.
- [62] Rashidi MM, Ali M, Freidoonimehr N, Nazari F. Parametric analysis and optimization of entropy generation in unsteady MHD flow over a stretching rotating disk using artificial neural network and particle swarm optimization algorithm. *Energy* 2013;55:497–510. <https://doi.org/10.1016/j.energy.2013.01.036>.
- [63] Penkuhn M, Tsatsaronis G. Exergy Analysis of the Allam Cycle. 5th Int Symp - Supercrit CO2 Power Cycles 2016:1–18.
- [64] Rogalev A, Grigoriev E, Kindra V, Rogalev N. Thermodynamic optimization and equipment development for a high efficient fossil fuel power plant with zero emissions. *J Clean Prod* 2019;236:117592. <https://doi.org/10.1016/j.jclepro.2019.07.067>.
- [65] Rodríguez Hervás G, Petrakopoulou F. Exergoeconomic Analysis of the Allam Cycle. *Energy Fuels* 2019;33:7561–8. <https://doi.org/10.1021/acs.energyfuels.9b01348>.
- [66] Allam R, Martin S, Forrest B, Fetvedt J, Lu X, Freed D, et al. Demonstration of the Allam Cycle: An Update on the Development Status of a High Efficiency Supercritical Carbon Dioxide Power Process Employing Full Carbon Capture. *Energy Procedia* 2017. <https://doi.org/10.1016/j.egypro.2017.03.1731>.
- [67] Chan W, Lei X, Chang F, Li H. Thermodynamic analysis and optimization of Allam cycle with a reheating configuration. *Energy Convers Manag* 2020;224:113382. <https://doi.org/10.1016/j.enconman.2020.113382>.
- [68] Xu C, Zhang Q, Yang Z, Li X, Xu G, Yang Y. An improved supercritical coal-fired power generation system incorporating a supplementary supercritical CO2 cycle. *Appl Energy* 2018. <https://doi.org/10.1016/j.apenergy.2018.09.122>.
- [69] Novales D, Erkoreka A, De la Peña V, Herrazti B. Sensitivity analysis of supercritical CO2 power cycle energy and exergy efficiencies regarding cycle component efficiencies for concentrating solar power. *Energy Convers Manag* 2019;182:430–50. <https://doi.org/10.1016/j.enconman.2018.12.016>.
- [70] Moissetsev A, Sienicki JJ. Transient accident analysis of a supercritical carbon dioxide Brayton cycle energy converter coupled to an autonomous lead-cooled fast reactor. *Nucl Eng Des* 2008;238:2094–105. <https://doi.org/10.1016/j.nucengdes.2007.11.012>.
- [71] Luo D, Huang D. Thermodynamic and exergoeconomic investigation of various SCO2 Brayton cycles for next generation nuclear reactors. *Energy Convers Manag* 2020;209:112649. <https://doi.org/10.1016/j.enconman.2020.112649>.
- [72] Akbari AD, Mahmoudi SMS. Thermo-economic analysis & optimization of the combined supercritical CO2 (carbon dioxide) recompression Brayton/organic Rankine cycle. *Energy* 2014;78:501–12. <https://doi.org/10.1016/j.energy.2014.10.037>.
- [73] Zhang F, Liao G, E J, Chen J, Leng E, Sundén B. Thermodynamic and exergoeconomic analysis of a novel CO2 based combined cooling, heating and power system. *Energy Convers Manag* 2020;222:113251. <https://doi.org/10.1016/j.enconman.2020.113251>.
- [74] Fan G, Li H, Du Y, Zheng S, Chen K, Dai Y. Preliminary conceptual design and thermo-economic analysis of a combined cooling, heating and power system based on supercritical carbon dioxide cycle. *Energy* 2020;203:117842. <https://doi.org/10.1016/j.energy.2020.117842>.
- [75] Noaman M, Saade G, Morosuk T, Tsatsaronis G. Exergoeconomic analysis applied to supercritical CO2 power systems. *Energy* 2019;183:756–65. <https://doi.org/10.1016/j.energy.2019.06.161>.
- [76] Yang Y, Huang Y, Jiang P, Zhu Y. Multi-objective optimization of combined cooling, heating, and power systems with supercritical CO2 recompression Brayton cycle. *Appl Energy* 2020. <https://doi.org/10.1016/j.apenergy.2020.115189>.
- [77] Sifat NS, Haseli Y. Thermodynamic modeling of Allam cycle. *ASME Int Mech Eng Congr Expo Proc* 2018;6A–144113:1–5. <https://doi.org/10.1115/IMECE2018-88079>.
- [78] Zhu Z, Chen Y, Wu J, Zhang S, Zheng S. A modified Allam cycle without compressors realizing efficient power generation with peak load shifting and CO2 capture. *Energy* 2019;174:478–87. <https://doi.org/10.1016/j.energy.2019.01.165>.
- [79] Zhu HH, Wang K, He YL. Thermodynamic analysis and comparison for different direct-heated supercritical CO2 Brayton cycles integrated into a solar thermal power tower system. *Energy* 2017;140:144–57. <https://doi.org/10.1016/j.energy.2017.08.067>.
- [80] Guo JQ, Li MJ, He YL, Xu JL. A study of new method and comprehensive evaluation on the improved performance of solar power tower plant with the CO2-based mixture cycles. *Appl Energy* 2019;256:113837. <https://doi.org/10.1016/j.apenergy.2019.113837>.
- [81] Wang K, Li MJ, Guo JQ, Li P, Bin Liu Z. A systematic comparison of different S-CO2 Brayton cycle layouts based on multi-objective optimization for applications in solar power tower plants. *Appl Energy* 2018;212:109–21. <https://doi.org/10.1016/j.apenergy.2017.12.031>.
- [82] Wang K, He YL, Zhu HH. Integration between supercritical CO2 Brayton cycles and molten salt solar power towers: A review and a comprehensive comparison of different cycle layouts. *Appl Energy* 2017;195:819–36. <https://doi.org/10.1016/j.apenergy.2017.03.099>.
- [83] Kim S, Cho Y, Kim MS, Kim M. Characteristics and optimization of supercritical CO2 recompression power cycle and the influence of pinch point temperature difference of recuperators. *Energy* 2018;147:1216–26. <https://doi.org/10.1016/j.energy.2017.12.161>.
- [84] Cengel YA, Boles MA. Thermodynamics: an Engineering Approach 8th Edition. 2015. [10.1017/CBO9781107415324.004](https://doi.org/10.1017/CBO9781107415324.004).
- [85] Jing Q, Xie Y, Zhang D. Thermal hydraulic performance of printed circuit heat exchanger with various channel configurations and arc ribs for SCO2 Brayton cycle. *Int J Heat Mass Transf* 2020;150:119272. <https://doi.org/10.1016/j.ijheatmasstransfer.2019.119272>.
- [86] Chai L, Tassou SA. Numerical study of the thermohydraulic performance of printed circuit heat exchangers for supercritical CO2 Brayton cycle applications. *Energy Procedia* 2019;161:480–8. <https://doi.org/10.1016/j.egypro.2019.02.066>.
- [87] Hesselgreaves, J E, Law R, Reay D. Compact Heat Exchangers, Selection, Design, and Operation. 2nd Editio. Butterworth-Heinemann; 2016.
- [88] Serrano IP, Cantizano A, Linares JI, Moratilla BY. Modeling and sizing of the heat exchangers of a new supercritical CO2 Brayton power cycle for energy conversion for fusion reactors. *Fusion Eng Des* 2014;89:1905–8. <https://doi.org/10.1016/j.fusengdes.2014.04.039>.
- [89] Penkuhn M, Tsatsaronis G. Exergy Analysis of the Allam Cycle. 5th Int. Symp. - Supercrit. CO2 Power Cycles, Texas 2016:1–18.
- [90] Ma Y, Morosuk T, Luo J, Liu M, Liu J. Superstructure design and optimization on supercritical carbon dioxide cycle for application in concentrated solar power plant. *Energy Convers Manag* 2020;206:112290. <https://doi.org/10.1016/j.enconman.2019.112290>.
- [91] Thanganadar D, Asfand F, Patchigolla K. Thermal performance and economic analysis of supercritical Carbon Dioxide cycles in combined cycle power plant. *Appl Energy* 2019;255:113836. <https://doi.org/10.1016/j.apenergy.2019.113836>.
- [92] Mohammadi K, Ellingwood K, Powell K. A novel triple power cycle featuring a gas turbine cycle with supercritical carbon dioxide and organic Rankine cycles: Thermo-economic analysis and optimization. *Energy Convers Manag* 2020;220:113123. <https://doi.org/10.1016/j.enconman.2020.113123>.
- [93] Ricardo M. CO2 capture in power plants-using the oxy-combustion principle. Norway: Norwegian University of Science and Technology; 2013.